Photoluminescence Studies of Polytype Heterostructured InP Nanostructures

Jash, Asmita

2024

Document Version:
Publisher's PDF, also known as Version of record

Photoluminescence Studies of Polytype Heterostructured InP Nanostructures

ASMITA JASH
DEPARTMENT OF SOLID STATE PHYSICS | FACULTY OF ENGINEERING | LUND UNIVERSITY

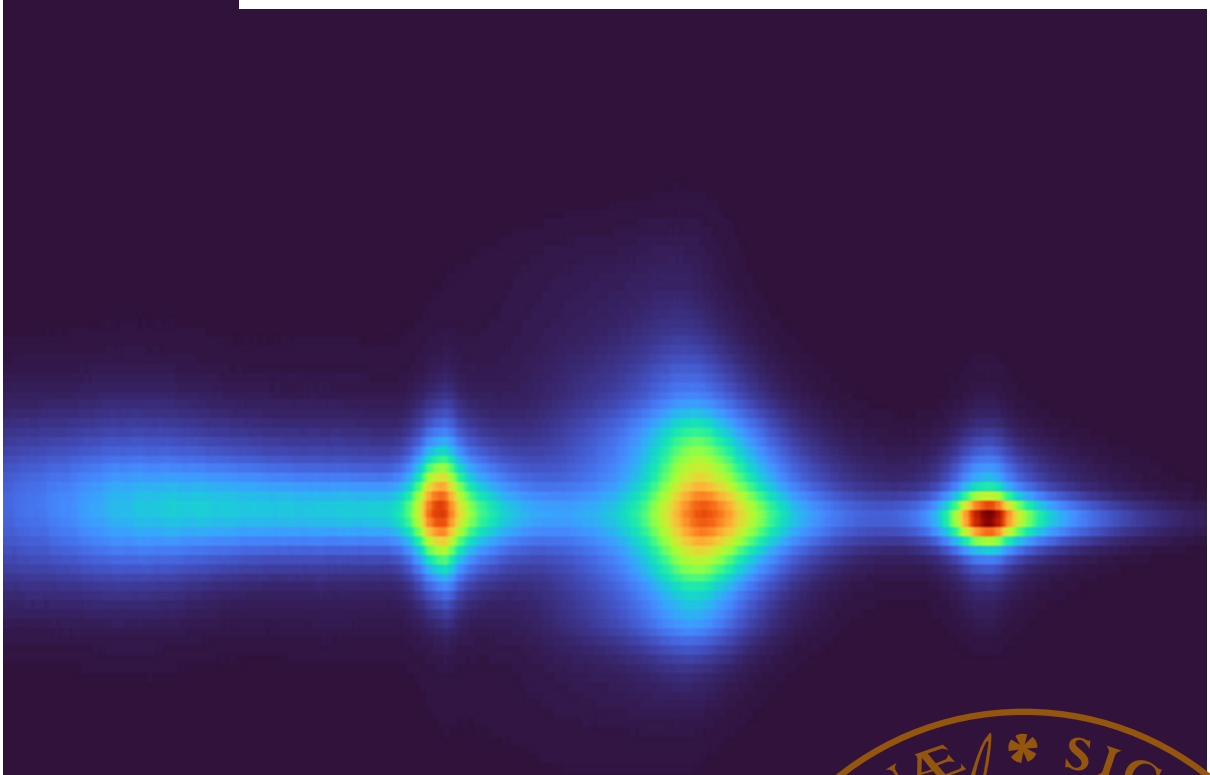

Printed by Media-Tryck, Lund 2024 NORDIC SWAN ECOLABEL 3041 0903

Faculty of Engineering, LTH
Department of Solid State Physics

ISBN 978-91-8039-966-1

Photoluminescence Studies of Polytype Heterostructured InP Nanostructures

Photoluminescence Studies of Polytype Heterostructured InP Nanostructures

By Asmita Jash

LUND
UNIVERSITY

DOCTORAL DISSERTATION

Doctoral dissertation for the degree of Doctor of Philosophy (PhD) at the Faculty of Engineering at Lund University to be publicly defended on Friday, the 22nd of March 2024, at 13:15 in the Rydberg Lecture Hall at the Department of Physics, Lund.

Faculty opponent
Prof. Sebastian Lourdudoss
KTH Royal Institute of Technology

Organization:
LUND UNIVERSITY
Department of Solid State Physics
Box 118
SE–221 00 LUND
Sweden

Document name: DOCTORAL DISSERTATION
Date of disputation: 2024-03-22
Sponsoring organization:

Author(s): Asmita Jash

Title and subtitle: Photoluminescence Studies of Polytype Heterostructured InP Nanostructures

Abstract: The interface between two semiconductors significantly influences their optical and electronic properties. In contrast to traditional material heterostructures, polytype heterostructures between wurtzite (wz) and zincblende (zb) segments in homomaterial InP nanostructures exhibit sharp interfaces with minimal strain. The wz/zb interface of heterostructured InP has a type-II band alignment, which results in the accumulation of charge carriers on either side of the interface, electrons on one side and holes on the other side. This separation leads to the formation of spatially separated (indirect) excitons (IXs) at the interface. This thesis focuses on studying the spatial and temporal recombination characteristics of IXs in these polytypic heterostructures in InP nanostructures. Two types of nanostructures, nanowires (NWs) and platelets, are employed to investigate single type-II wz/zb interfaces. NWs have cylindrical or hexagonal cross-sections with a very small diameter and longer length, resulting in a small interface cross section (< 1 mm^2) while platelets on the other hand are characterized by much larger interface areas (> 500 mm^2).

The methodology in this thesis utilizes non-invasive optical techniques, specifically steady-state (SS) and time-resolved (TR) photoluminescence (PL) to analyze the emission spectra of InP polytype heterostructures. The confirmation of a type-II band alignment is established through excitation power density (EPD)-dependent SSPL, where the IX emission redshifts with reduced EPD. In addition, the TRPL data reveals a long lived and non-exponential decay profile of the IX emission.

Paper-I delves into the recombination dynamics of IXs at the single wz/zb interface in InP NWs. Overcoming the small cross-section limitation of NWs, platelets, with a substantially larger cross-section, provide a larger sample area and, thus, provides access to investigating the transport of IXs. Paper-II and Paper-III explore the IX dynamics at the wz/zb single-interface of platelets. Spatially resolved SSPL in undoped platelets unveils EPD-dependent transport of IXs at the type-II interface. The broad spatial distribution of the IX emission suggests repulsive-force-driven transport at high EPD, while the narrow spatial distribution at low EPD indicates a diffusive transport mechanism. The temporal evolution, observed through spatially resolved TRPL, depicts an initial rapid expansion of the IXs driven by Coulomb repulsion - a result of the dipole alignment of the IXs at the interface. After this initial step, it is transitioning to a linear expansion indicative of diffusive-driven transport in undoped platelets. This behavior is characteristic for a low scattering of IXs which is indicative of a minor impact of interface fluctuations caused by the polytype interface in our system.

Beyond characterizing undoped nanostructures, our research explores the impact of a two-dimensional electron gas (2DEG) on the recombination and spatial dynamics of IXs for n-type doped nanostructures. These doped structures maintain the same geometry as the undoped counterparts, except for the n-type doping applied to the entire wz segment. Doped samples exhibit a smaller redshift with reduced EPD and shorter recombination times for IX emission compared to the undoped ones. Additionally, the spatial distribution of IX emission is independent of EPD.

Key words: III-V semiconductor, Photoluminescence, Time-Resolved Photoluminescence, Polytype, Crystal phase heterostructure, InP, Wurtzite, Zincblende, Indirect Exciton

Classification system and/or index terms (if any)

Supplementary bibliographical information

Language: English

ISSN and key title:

ISBN: 978-91-8039-966-1 (print)
978-91-8039-967-8 (electronic)

Recipient's notes

Number of pages: 90

Price

Security classification

Signature

Date 2024-02-27

Photoluminescence Studies of Polytype Heterostructured InP Nanostructures

Asmita Jash

LUND
UNIVERSITY

Cover illustration front: An artistic rendition of spatially resolved photoluminescence spectra from a wurtzite-zincblende InP heterostructure platelet.

Faculty of Engineering, LTH, Department of Solid State Physics
ISBN 978-91-8039-966-1 (print)
ISBN 978-91-8039-967-8 (electronic)

Printed in Sweden by Media-Tryck, Lund University
Lund 2024

জ্ঞান যেন থাকে মুক্ত শৃঙ্খলাবিহীন
- রবীন্দ্রনাথ ঠাকুর

Table of Contents

Abstract ..... **i**

Popular scientific description ..... **iii**

List of Papers ..... **vi**

Acknowledgments ..... **viii**

Abbreviations ..... **x**

1 Introduction **1**

2 Theory **5**

2.1 Semiconductors 5

2.1.1 Band Structure 5

2.1.2 Excitons 7

2.2 Semiconductor Heterostructures 9

2.2.1 Polytypism 10

2.2.2 Nanostructures 14

2.3 Recombination Dynamics 16

2.4 Indirect Exciton Transport 21

3 Experimental Methods **23**

3.1 Growth 23

3.1.1 Particle-Assisted Nanowire Growth 24

3.1.2 Selective Area Platelet Growth 26

3.2 Photoluminescence Spectroscopy 27

3.2.1 Steady-State Photoluminescence Spectroscopy 29

3.2.2 Time-resolved Photoluminescence Spectroscopy 30

3.2.2.1 Time-correlated single-photon counting 30

3.2.2.2 Streak Systems 32

3.3 Local & Spatial Detection 35

3.3.1 Steady-state Photoluminescence Spectroscopy 35

3.3.2 Time-resolved Photoluminescence Spectroscopy 37

3.4 Scanning Electron Microscopy 40

3.5 Sample Preparation 41

4 Results.....43
4.1 Heterostructured InP Nanowires 43
4.1.1 Undoped wz/zb InP nanowires.....44
4.1.2 n-type doped wz/zb InP nanowires 47
4.2 Heterostructured InP Platelets 49
4.2.1 Steady-state Photoluminescence 50
4.2.2 Time-resolved Photoluminescence.....52
4.2.3 Spatially Resolved Steady-State Photoluminescence.....56
4.2.4 Spatially Resolved Time-resolved Photoluminescence.....59
Conclusion & Outlook.....63
References 67

Abstract

The interface between two semiconductors significantly influences their optical and electronic properties. In contrast to traditional material heterostructures, polytype heterostructures between wurtzite (wz) and zincblende (zb) segments in homomaterial InP nanostructures exhibit sharp interfaces with minimal strain. The wz/zb interface of heterostructured InP has a type-II band alignment, which results in the accumulation of charge carriers on either side of the interface, electrons on one side and holes on the other side. This separation leads to the formation of spatially separated (indirect) excitons (IXs) at the interface. This thesis focuses on studying the spatial and temporal recombination characteristics of IXs in these polytypic heterostructures in InP nanostructures. Two types of nanostructures, nanowires (NWs) and platelets, are employed to investigate single type-II wz/zb interfaces. NWs have cylindrical or hexagonal cross-sections with a very small diameter and longer length, resulting in a small interface cross section ($< 1\ \mu m^2$) while platelets on the other hand are characterized by much larger ($> 500\ \mu m^2$) interface areas.

The methodology in this thesis utilizes non-invasive optical techniques, specifically steady-state (SS) and time-resolved (TR) photoluminescence (PL) to analyze the emission spectra of InP polytype heterostructures. The confirmation of a type-II band alignment is established through excitation power density (EPD)-dependent SSPL, where the IX emission redshifts with reduced EPD. In addition, the TRPL data reveals a long lived and non-exponential decay profile of the IX emission.

Paper-I delves into the recombination dynamics of IXs at the single wz/zb interface in InP NWs. Overcoming the small cross-section limitation of NWs, platelets, with a substantially larger cross-section, provide a larger sample area and, thus, provides access to investigating the transport of IXs. Paper-II and Paper-III explore the IX dynamics at the wz/zb single-interface of platelets. Spatially resolved SSPL in undoped platelets unveils EPD-dependent transport of IXs at the type-II interface. The broad spatial distribution of the IX emission suggests repulsive-force-driven transport at high EPD, while the narrow spatial distribution at low EPD indicates a diffusive transport mechanism. The temporal evolution, observed through spatially resolved TRPL, depicts an initial rapid expansion of the IXs driven by Coulomb repulsion - a result of the dipole alignment of the IXs at the interface. After this initial step, it is transitioning to a linear expansion indicative of diffusive-driven transport in undoped platelets. This behavior is characteristic for a low scattering of

IXs which is indicative of a minor impact of interface fluctuations caused by the polytype interface in our system.

Beyond characterizing undoped nanostructures, our research explores the impact of a two-dimensional electron gas (2DEG) on the recombination and spatial dynamics of IXs for n-type doped nanostructures. These doped structures maintain the same geometry as the undoped counterparts, except for the n-type doping applied to the entire wz segment. Doped samples exhibit a smaller redshift with reduced EPD and shorter recombination times for IX emission compared to the undoped ones. Additionally, the spatial distribution of IX emission is independent of EPD.

Popular scientific description

In our everyday lives, we encounter a variety of essential tools and technologies. For instance, we rely on smartphones for communication and light-emitting diode (LED) lights for brightening our homes. These useful gadgets, including computers, tablets, and smartphones, are powered by integrated circuits (ICs) containing billions of tiny switches called transistors. These transistors act as controllers of electrical flow, enabling the devices to process information swiftly and effectively. Beyond these common devices, there are others that utilize a combination of light and electricity to fulfill their purposes such as cameras, LED lighting, and fiber optical communication systems. Cameras utilize light-sensitive sensors to capture images by converting incoming light into electrical signals, while LED lighting relies on the efficient conversion of electrical energy into light. Fiber optical communication systems transmit data using short light pulses, enabling high-speed and reliable communication over long distances. These fascinating technologies all rely on semiconductors as their core building blocks. Semiconducting materials have unique properties that can be engineered and manipulated to meet specific requirements. They are essential for creating these various components like transistors and optoelectronic devices. For example, LEDs utilize semiconductors to emit light when a voltage is applied, without the need for heating, unlike incandescent light sources. Similarly, solar cells use semiconductors to convert sunlight into electrical energy, thereby enabling the generation of clean and renewable power.

The constant pursuit of faster and more efficient devices has led to the necessity of scaling down individual semiconductor components to the micro and nanoscale. In our everyday lives, we are familiar with the macro scale, where objects are visible to the naked eye and measured in units such as meters or centimeters. However, the microscale is approximately a million times smaller than what we commonly observe, and the nanoscale is a billion times smaller. To put this into perspective, consider the width of a human hair, which measures around 100 micrometers (μm). At the nanoscale, objects are even smaller, such as a single strand of DNA, which is a mere 2.5 nanometers (nm) wide. The properties of materials undergo significant changes at such microscopic sizes, diverging from those observed at the macro scale. These differences in properties have a profound impact on the performance of devices.

The core of the discussed devices lies in a category of materials known as semiconductors. In their pure form, these materials are rather unremarkable, as they are not especially good at conducting current and they are not good electrical insulators either. What makes these materials great is that we can change their properties by adding impurities, called doping. Doping can introduce additional electrons, but also their positively charged counterpart, holes. When an electron meets a hole, light may be emitted. The color of the light depends on the semiconductor material. When we shine light on a semiconductor, an electron and a hole can be created. This effect is used for instance in solar cells. Combining various semiconductors can be incredibly useful when creating unique structures known as heterostructures. These heterostructures are formed by stacking different semiconductor materials on top of one another. Take, for instance, an LED constructed using a heterostructure composed of multiple semiconductor layers. When we power up an LED by applying a voltage, electrons from one side of the LED are pushed to the center, where they meet holes pushed from the other side. Adjusting the thickness and composition of the layer where they meet, we can control the colors of the light produced. Such engineering allows us to create common LED colors like vibrant blue and sunny yellow, covering the entire spectrum of the rainbow.

In this thesis, the focus is on studying a specific type of heterostructure known as polytype semiconductor heterostructures. They are made using the same semiconductor material but with different crystal structures. The crystal structure of a material refers to how its atoms are arranged in a repeating pattern, and it has a significant impact on the properties of the semiconductor. Within the same semiconductor material, there can be different crystal structures. An example is carbon which can be either diamond or graphite. Despite having the same chemical composition, different crystal phases can exhibit distinctly different properties. By utilizing polytype heterostructures, it becomes possible to create heterostructures using only a single material. This is different from traditional heterostructures that are formed by combining different semiconductors including associated challenges.

The specific semiconductor material explored in this thesis is indium phosphide (InP). Depending on the growth conditions, InP can exhibit different crystal structures. In its bulk form, it has a crystal structure called zincblende (zb). However, when grown as nanostructures, it can adopt a different crystal structure called wurtzite (wz). By controlling the growth parameters, we can switch between these crystal structures and grow pure crystalline materials. The interfaces between the different crystal structures in polytype heterostructures are very promising for both fundamental research and novel applications in the field of semiconductor materials. This interface causes electrons to be confined to the zb side of the interface while holes are confined to the wz side. To comprehend the physical processes in semiconductor InP nanostructures, we employ photoluminescence spectroscopy, a non-destructive method. This technique entails illuminating a

material, measuring the color and intensity of the emitted light, and thereby gaining insights into the properties of materials. In this thesis, we utilize this approach to analyze the spatial distribution and recombination dynamics of electron-holes. These aspects are crucial for comprehending electronic processes at polytype heterostructures and, consequently, identifying potential applications.

List of Papers

Publications included in the thesis:

Paper I

Time-resolved photoluminescence studies of single interface wurtzite/zincblende heterostructured InP nanowires

A. Jash, A. Yangui, S. Lehmann, I.G. Scheblykin, K.A. Dick, A. Gustafsson, M. E. Pistol.

Appl. *Phys. Lett.* **120**, 113102 (2022).

I took part in project planning, performed the optical measurements and data analysis, and took the leading role in the preparation of the manuscript and the revision.

Paper II

Excitonic Dynamics at the type-II Polytype Interface of InP Platelets

A. Jash, S. Lehmann, K.A. Dick, A. Gustafsson, M. E. Pistol.

ACS Photonics **10**, 9 (2023).

I took part in project planning and performed optical measurements and data analysis. I developed spatial imaging and time-resolved measurements. I took the leading role in the preparation of the manuscript and the revision.

Paper III

Transport of Dipolar Excitons at the type-II Polytype Interface of InP Platelets

A. Jash, S. Lehmann, K.A. Dick, A. Gustafsson, M. E. Pistol.

Manuscript to be submitted

I took part in project planning and performed optical measurements and data analysis. I developed the time-resolved measurements further. I took the leading role in the preparation of the manuscript.

Publication beyond the scope of this thesis:

Paper IV

Atomic Hydrogen Annealing of Graphene on InAs Surfaces and Nanowires: Interface and Morphology Control for Optoelectronics and Quantum Technologies

S. F. Mousavi, Y. Liu, G. D'Acunto, A. Troian, J. M. Caridad, Y. Niu, L. Zhu, A. Jash, V. Flodgren, S. Lehmann, K.A. Dick, A. Zakharov, R. Timm, and A. Mikkelsen.

ACS Appl. Nano Mater. ***5****, 12 (2022).*

Acknowledgments

As my five-year PhD journey comes to a close, I wish to express my gratitude to the many individuals whose presence throughout this time has made this journey a great developmental experience for me, both academically and personally. While it is impossible to acknowledge everyone who has contributed to my journey, I want to make an attempt to do so.

It brings me great joy to extend my sincerest gratitude to Anders Gustafsson, my main supervisor, for his invaluable support and guidance throughout my PhD journey. Thank you for entrusting me with the opportunity to work as a PhD student. Your constructive feedback has not only helped me refine my work but has also contributed significantly to my professional growth. I would also like to express my sincere gratitude to my co-supervisors, Mats-Erik Pistol and Sebastian Lehmann. Mats-Erik, your profound scientific knowledge and keen interest have been invaluable to the progress of the projects. Sebastian, I appreciate your willingness to assist me when I face challenges in the lab or while writing. Your mentorship, drawn from your research experiences has greatly aided me in managing my tasks effectively. I would also like to express my gratitude to Ivan G. Scheblykin and Aymen Yangui for their collaboration and contributions to the project.

When I first arrived at the lab, I felt overwhelmed by the multitude of unfamiliar optical instruments and doubted how I would manage to learn them all. However, thanks to the guidance from Neimantas and Irene, I gained knowledge about the PL setup. I owe a debt of gratitude to Dan Hessman for his invaluable support with the TRPL setup. His eager assistance with equipment-related issues, as well as the discussions with him about the project, have played a pivotal role in advancing this project. I am also grateful to Steffen for his willingness to offer help with lab setup and to Anders Persson for his readiness to solve any problems related to the laser.

I want to extend my appreciation to Adam Bruke, Alexander den Ouden, Bengt Meuller, and Anders Kvennefors for being available whenever I reach out for help in the lab. I am also deeply grateful for the technical and administrative assistance I received from all the FTF staff. I extend my heartfelt thanks to Alfons Eriksson, Andreas Bergelin, Anna Levin, Håkan Lapovski, Marica Kolobaric, and Mirja Carlsson Möller for their support.

I have had the delightful opportunity to become acquainted with numerous PhD students, making friends along the way. Among them are the trio - Antti, Hossein,

and Kristi, as well as Marie, Anette, Twinkle, Yue, David, Pradheeba, Therese, Subhomoy….and the list goes on. Thanks to Arti and Monalisa for listening to all my complaints when things were not working.

I wish to express my deepest appreciation to my parents in India, who have stood by me. Thank you for providing me with constant moral and emotional support throughout these years.

Abbreviations

2DEG	Two-dimensional electron gas
APD	Avalanche photodiode
CB	Conduction band
CCD	Charge-coupled device
CCP	Cubic close-packed
CW	Continuous wave
E_c	Conduction band energy
E_d	Donor level
E_F	Fermi-level
E_g	Bandgap energy
EPD	Excitation power density
$E_{type-II}$	type-II transition energy
E_v	Valence band energy
FCC	Face centered cubic
GaAs	Gallium arsenide
H_2S	Hydrogen sulfide
HCP	Hexagonal close-packed
InP	Indium phosphide
IX	Indirect exciton
LED	Light emitting diode
MCP	Microchannel plate
MOVPE	Metalorganic vapor-phase epitaxy
NA	Numerical aperture
ND	Neutral Density
NW	Nanowire
PC	Photocathode
PH_3	Phosphine
PL	Photoluminescence

QW	Quantum well
S	Sulphur
SAG	Selective area growth
SEM	Scanning electron microscopy
SiN_X	Silicon nitride
SSPL	Steady-state Photoluminescence
SEM	Scanning electron microscopy
TCSPC	Time-Correlated Single Photon Counting
Ti:Sa	Titanium sapphire
TMIn	Trimethylindium
TRPL	Time-resolved Photoluminescence
VB	Valence band
VLS	Vapor-liquid-solid
wz	Wurtzite
zb	Zincblende

1 Introduction

Semiconductors play a vital role in driving modern technological advancements. They serve as the foundation for optoelectronic and electronic devices such as solar cells[1], light-emitting diodes (LEDs)[2], and transistors[3,4]. To make further advancements in these devices, it has become essential to increase the number of transistors that can be placed on an integrated circuit, resulting in better, faster, and more efficient devices[5]. This requires further downsizing of the transistors. Recent developments in the fabrication of high-quality materials have made it possible to scale down the size of devices to the nanometer scale[6]. The ability to manipulate the size and structures of semiconductors at the nanometer scale can significantly alter the material properties. Additionally, physical phenomena in nanostructured materials have attracted scientific interest due to their potential to provide a platform for the study of materials with unique properties.

In this thesis, the optical properties of a III-V binary semiconductor, namely InP, are investigated. III-V semiconductors are a class of semiconductor compounds that consist of atoms from group III and group V of the periodic table. Many III-V semiconductors have a direct electronic bandgap, which makes them highly efficient absorbers and emitters- properties that are essential for optoelectronic devices[7]. Moreover, within these material systems, the capacity to fabricate various alloy combinations confers the capability for bandgap engineering spanning a wide range of energies. This affords the precise customization of material characteristics tailored to device applications[3]. As an illustrative instance, the bandgap may be finely adjusted to enable LEDs to emit light across the spectrum, ranging from Infrared (IR) to Ultraviolet (UV) wavelengths[8].

Heterostructured semiconductors made from a combination of different semiconductors with different bandgaps offer the possibility of creating optoelectronic devices with tuned spectral characteristics and efficient performance. The band alignment across a heterostructure interface can be classified into three categories: type-I, type-II, and type-III[9]. This thesis focuses on type-II band alignment, characterized by a staggered band arrangement where both the valence and conduction band edges in one semiconductor are higher than their counterparts in the other semiconductor. In a type-II band alignment, the presence of a potential step at the heterointerface prevents the diffusion of charge carriers (electrons and holes) across the interface, leading to their spatial separation. As a consequence of this spatial separation, charge carriers tend to accumulate on either side of the

interface, attracted to one another by the Coulomb force. This accumulation of charge carriers leads to band-bending at the interface, resulting in the formation of approximately triangular potential wells on both sides of the interface[10]. The type-II band alignment has been studied in detail in various III-V materials systems, such as InAlAs/InP[11], GaAs/AlAs[12], GaInAsSb/GaSb[13], but also in polytype heterostructures like GaAs[14] and InP[15]. In polytype heterostructures, it is even possible to create a two-dimensional electron gas (2DEG) in the triangular potential well formed at the type-II interface by modulation doping[16]. This will be discussed further in chapter two.

Polytype heterostructures are made from the same material by switching only the crystal structure and they provide a promising opportunity for optoelectronic materials in comparison to conventional heterostructures made from different materials. The presence of defects such as interface roughness and compositional intermixing in conventional heterostructures can affect the optical and transport properties significantly[17]. For instance, in light-emitting devices, such as LEDs or lasers, interface roughness, and compositional intermixing can lead to non-uniform light emission, reduced brightness, and lower external quantum efficiency[18,19]. Interface roughness introduces irregularities at the interface between different materials, which can result in a broadening of the optical spectrum. Additionally, the presence of compositional intermixing can alter the band structure and electronic properties of the heterostructure, affecting the ability to emit light efficiently[20]. These defects have an impact on the performance of various optoelectronic applications. In polytype heterojunctions, however, sharp interfaces and negligible strain can indeed be achieved. Made from the same compound, such as zincblende (zb) and wurtzite (wz) GaAs or InP[21], different bandgaps and band offsets of the zb and wz crystal phases create a polytype wz/zb heterostructure. The zb crystal structure is the thermodynamically stable phase for bulk material of most III-V semiconductors (except the III-Nitrides). However, in nanostructured forms, these semiconductors can be grown in the wz crystal phase. With the advancement of suitable growth methods and conditions, we have the ability to grow nanostructures with either pure wz or zb crystal structure, and even controllably switch between the two polytypes with high accuracy and sharp interfaces[22]. This has opened up many possibilities for the design and growth of polytype wz/zb heterostructures.

The previously mentioned wz/zb InP heterostructure provides an opportunity to explore the dynamics of both charge carriers (or direct and indirect excitons) following the excitation of the nanostructure. Direct excitons refer to Coulomb-bound electron-hole pairs within the same material. Indirect excitons (IX) are Coulomb-bound electron-hole pairs that are confined in spatially separated potential wells at the type-II interface[23]. The special case of the polytype type-II interface which acts as a separator of electrons and holes, provides a unique opportunity to study the formation of IXs. Unlike direct excitons, which can recombine and emit light on a short time scale, IXs have a long recombination time[24]. In order to

elucidate the optical properties of type-II interfaces, we have employed non-destructive photoluminescence (PL) spectroscopy to obtain emission spectra from photo-excited nanostructures[25]. This has provided insights into the dominant emission from the materials as well as the crystal quality. Furthermore, we have used time-resolved photoluminescence (TRPL) spectroscopy to study the recombination dynamics of excitons after pulsed excitation which enabled us to record the temporal decay profile of the emission[26]. In the thesis, we examined two kinds of polytype wz/zb InP nanostructures: nanowires (NWs) and platelets.

NWs are quasi-one-dimensional structures that have cylindrical or hexagonal cross-sections with a very small diameter (typically in the nanometer range) and a significantly longer length (typically in the micrometer range) that can be several orders of magnitude larger than its diameter[27,28]. While there are numerous publications on structural and optical properties of heterostructured NWs[29-31], there have been limited investigations into the recombination kinetics of IXs at the single polytype type-II interfaces, possibly due to the scarcity of heterostructures with pure crystal phases.

In the first project presented in this thesis, we investigated two different types of NW samples using optical measurements. The first type is the nominally undoped single heterojunction interface in wz/zb NWs. The second type shares an identical geometry, with the distinction that the entire wz segment is n-type doped. This aims to investigate the impact of the presence of a 2DEG at a wz/zb type-II interface on the emission characteristics and recombination time of excitons. To confirm the presence of a type-II interface in both types, we performed power-dependent PL measurements. A notable feature of IX emission is its redshift as the laser excitation power density (EPD) decreases. We also used TRPL to investigate the recombination dynamics of IXs in both types of NWs. Our PL and TRPL results show that the EPD dependence of the IX emission differs between the undoped and n-type doped NWs. Furthermore, our TRPL measurements reveal that a significant amount of intensity of the IX emission remains after 30 ns for the undoped NWs, which is a result of the spatially separated charge carriers at the interface. At the same time, we obtained a short recombination time (sub-ns) for the direct excitons in both the wz and zb segments.

This long recombination time of IXs is advantageous to facilitate the transport of IXs over substantial distances within the structure[32]. The long-lived IXs are also a suitable system for exciton condensation[33]. The formation of these IXs results in the creation of dipoles that are oriented perpendicular to the interface and interact repulsively, expanding over a larger area than the actual excitation spot size of the excitation. To overcome the limitation of the small cross-section ($<< 1\ \mu m^2$) of NWs, we studied the spatial distribution of IXs along the type-II interface on InP platelets. The InP platelets consist of a large-area cross-section ($> 500\ \mu m^2$) of a thin, flat InP wz layer on top of a zb InP substrate, providing a significantly larger sample for studying the spatial distribution of IXs. Furthermore, the interface is

situated far away from the side surfaces, thereby mitigating the influence of surface defects on the emission of IXs.

In the second and third projects, we investigated the transport of IXs along the type-II interface in large-area wz/zb InP platelets using spatially and temporally resolved PL spectroscopy. Our experimental approach allowed us to study the spatial distribution and recombination dynamics of IXs along the type-II interface and interpret the underlying transport processes. Our observations indicate that a high density of dipolar IXs exhibits a large expansion driven by a strong repulsive force, dominating over diffusive mechanisms at high EPD, while the transport of IXs is dominated by diffusion at low EPD. In contrast, the transport of direct excitons in the wz and zb segments is diffusive and EPD-independent. Notably, TRPL measurements revealed a significant emission intensity of the long-lived IXs, which remains even 40 µs after pulse excitation. This is significantly longer than in the case of the NW, where competition from surface recombination is present. Additionally, we provide a comparative examination involving doped platelets in conjunction with their undoped counterparts. To enable the doping of polytype InP platelets, intentional n-type doping was introduced during the growth phase of the wz-segment. Notably, in the context of n-type doped platelets, discernible differences have been identified in the dependency of emission lines on EPD and recombination, as compared to undoped platelets.

The thesis is structured in the following manner: In chapter two, I present the theoretical background of semiconductors and their optical properties, both necessary for analyzing the experimental results. In chapter three, I detail the fabrication process of polytype InP nanostructures and describe the experimental methods used to characterize their optical properties. Chapter four is dedicated to presenting and analyzing the results obtained from PL and TRPL investigations of InP wz/zb heterostructures under different EPDs. Finally, in chapter five, I summarize the main conclusions drawn from our study and propose future research directions.

2 Theory

This chapter provides a brief overview of the key physics concepts employed in this thesis. The discussion is based on the fundamentals of semiconductor physics and charge carrier dynamics, as well as the zb and wz crystal structures approached from a crystallographic perspective, and their relevance for the present work.

2.1 Semiconductors

Most semiconductor materials are defined by their crystalline structure, which determines the arrangement of atoms within the material. This periodicity in the arrangement of atoms has a significant impact on the electronic properties of the semiconductor. The electronic properties are described by the band structure, which defines the energy levels that an electron can occupy within the semiconductor. In essence, all the transport and optical properties of a semiconductor are determined by its band structure[34].

2.1.1 Band Structure

When atoms are widely spaced, their electrons remain bound to their individual atoms (nuclei) without interacting with electrons from nearby atoms. This results in electrons having only discrete, quantized energy levels. Within an atom, electrons are organized into distinct energy levels or electron shells. The innermost shell contains the highest binding energy for electrons, while those in the outer shells have progressively lower binding energy. Electrons occupy the innermost shells before filling the outer shells due to their energy levels. In this way the total energy of the atom is minimized. According to the Pauli exclusion principle, each energy level can only accommodate two electrons with opposite spin. Atoms of the same element are identical, having the same number of electrons and energy levels. When two atoms come into proximity, their electrons interact. This interaction causes the single, initially discrete, quantized energy levels to split into two distinct energy levels because of the Pauli exclusion principle. In the process of solid formation, numerous individual atoms densely occupy a confined volume. Each atom experiences the potential energy arising from its neighboring atoms due to their proximity, and because these atoms are identical, their energy levels split into

multiple energy levels. These closely spaced multiple energy levels form continuous bands of energy. The energy band replaces the discrete energy levels found in individual atoms and is associated with the electrons originating from the atomic structure. These bands may exhibit either overlapping or non-overlapping characteristics, potentially creating regions on the energy scale without any energy levels. Electrons occupy the lower energy bands first. In metals, the highest energy band is partially filled, ensuring high electrical conductivity, as electrons can move freely within this energy band[5].

In the case of semiconductors and insulators at absolute zero (0 K) temperature, the highest band, which is completely filled, is termed the valence band (VB). While the higher energy bands, devoid of electrons (ignoring thermal excitations from the VB), constitute the conduction band (CB). Between these two bands: VB and CB, there exists a forbidden energy gap referred to as bandgap (E_g). At low temperatures, a completely filled VB restricts the movement of electrons due to the absence of unoccupied energy levels in the VB of the semiconductors. For electrons to move within the semiconductor, it is necessary to promote them from the VB to the CB using an external energy source, such as light, since there are unoccupied energy levels in the CB where electrons can move freely. Ultimately, the application of an external electric field can facilitate electron movement, enabling the conduction of electricity. The number of electrons transitioning from the VB to the CB at any temperature depends on the bandgap. The smaller the bandgap, the larger the number of electrons that can make an upward transition, and the larger the bandgap, the smaller their number. The magnitude of the bandgap fundamentally distinguishes between insulators and semiconductors. Insulators feature a larger bandgap, impeding electrical current flow at room temperature, as the thermal energy is insufficient to excite electrons from the VB to the CB over the large bandgap. Conversely, semiconductors with a smaller or moderate bandgap allow some electrons to populate the CB, enabling them to conduct current at room temperature. The boundary between insulators and semiconductors is not precisely defined. To determine the probability of electron occupation within these energy bands the term 'Fermi level (E_f)' is commonly utilized. This level marks the energy at which the electron occupancy probability is 50%. Generally, in semiconductors and insulators, the Fermi level is situated within the bandgap as shown in Fig 2.1(a).

Promoting electrons to the CB involves leaving behind an empty place in the VB called a hole. The term 'hole' refers to a theoretical concept known as a virtual particle. Despite its virtual nature, a hole exhibits a behavior akin to that of a particle, having a positive charge and mass-like characteristics. These holes conduct current in a manner similar to electrons but move in the opposite direction since they possess the opposite charge. The collective movement of both electrons and holes is responsible for conducting electrical current in a semiconductor. Within a semiconductor, electrons and holes adopt modified masses, giving rise to what is known as the effective mass. This effective mass characterizes the behavior of

charge carriers within the semiconductor, accounting for the influence of the crystal lattice on their motion[35].

Increasing the number of charge carriers (electrons or holes) in energy bands is essential to modify the conductivity of the materials. To achieve this, one can employ doping, which involves substituting a small number of atoms into the crystal lattice and introducing excess electrons (donors) or holes (acceptors). Doping introduces energy states within the bandgap, close to the VB for acceptors and close to the CB for donors. Materials doped with acceptor atoms are considered p-type doped, while those doped with donor atoms are considered n-type doped. In undoped, semi-insulating semiconductors, the Fermi level is situated approximately in the middle of the bandgap. However, when doped, the Fermi level shifts towards either the CB for n-type doping or the VB for p-type doping, as depicted in Fig 2.1(b) and Fig 2.1(c). With increased doping concentration, the Fermi level moves closer to the nearest band edge. In the case of high doping concentrations, the Fermi level aligns within one of the energy bands as shown in Fig 2.1(d), leading to a very high concentration of charge carriers. This type of doping is known as degenerate doping, and it significantly influences the electrical conductivity of the material[36].

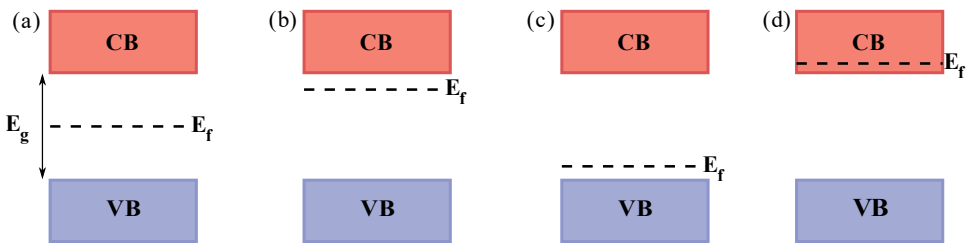

Figure 2.1: *Illustrated scheme showing the Fermi level position within the band gap in the case of (a) intrinsic, semi-insulating, (b) n-type, (c) p-type semiconductor, and (d) degenerate n-type doping.*

2.1.2 Excitons

Apart from electrons and holes, materials may also contain another type of carrier called excitons. When a photon with an energy greater than the material's bandgap excites the material, it has the potential to elevate an electron from the VB to the CB. The transition of an electron, induced by a photon, leaves behind a hole with an opposite electric charge. The electrostatic Coulomb interaction between the negatively charged electron and the positively charged hole can lead to the formation of an electron-hole pair known as an exciton. Excitons are characterized by the Bohr radius and binding energy. The 'Bohr radius' term is generally used in the hydrogen atom model. In the case of hydrogen, the Bohr radius is a fundamental constant denoting the most probable distance between the nucleus and electron in the ground state of a hydrogen atom. Applying the Bohr model to excitons, the Bohr

radius signifies the distance between the electron and the hole. For excitons, where the electron and hole move through a medium with a high dielectric constant, the Bohr radius is modified by the dielectric constant and the effective mass of the electron and hole. The Coulomb attraction between the electron and hole results in an exciton binding energy, leading to a transition energy slightly lower than the bandgap, as illustrated in Fig 2.2(c). This lower energy level positions the ground state for the electrons and holes of the exciton, distinct from the corresponding electron-hole pair in the VB-CB. The exciton binding energy in InP is approximately 5 meV[37]. Generally, the likelihood of exciton presence is higher at low temperatures. At room temperature, when the thermal energy (25 meV) surpasses the binding energy of excitons, they tend to dissociate into separate electrons and holes.

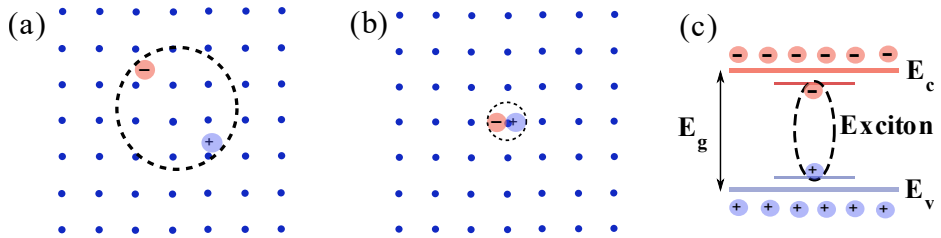

Figure 2.2: *Schematic of two types of excitons: (a) Wannier exciton and (b) Frenkel exciton. The light blue dots represent atoms of the media they exist in, and the blue and red circles represent the electron and hole respectively. (c) Bandgap of excitons.*

The properties of excitons depend on the material they form in, leading to two limiting cases:

1. **Frenkel Excitons:** These excitons have a relatively small Bohr radius compared to the lattice constant of the material. In solids with small dielectric constant, such as ionic crystals and organic or molecule semiconductors, the exciton is more tightly bound and is associated with a single atom, known as a Frenkel exciton[38].
2. **Wannier Excitons:** In this case, the Bohr radius is much larger than the lattice constant. The large dielectric constant (e.g., 12.5 for InP) in most semiconductors limits the Coulomb interaction between the electron and the hole. This leads to a large Bohr radius for semiconductor excitons, exceeding multiple lattice constants. In this regime, the excitons are referred to as Wannier excitons. A Wannier exciton can be effectively modeled as a hydrogen atom, with the Bohr radius and energy levels adjusted to account for differences in the effective masses of the electron and hole, as well as the permittivity of the material[38]. The Bohr radius for InP excitons is around 15 nm[39].

2.2 Semiconductor Heterostructures

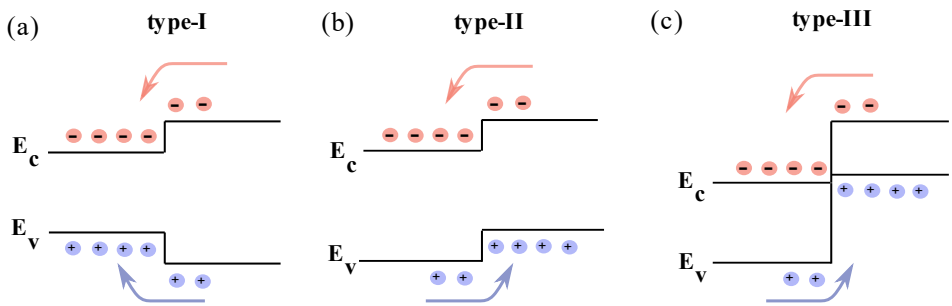

***Figure 2.3**: Examples of different heterostructure types: (a) type-I (straddling), (b) type-II (staggered), and (c) type-III (broken gap) alignment. The diffusion of the excited charge carriers is indicated by electrons and holes. The blue and red circles represent electrons and holes, respectively.*

It is possible to combine different semiconductors having electronic energy levels with different positions of the band edges to create semiconductor heterostructures[40]. The beneficial properties of different semiconductors in heterostructures have enabled progress in electronics and optoelectronics. One such advantage is the possibility to create structures with quantum confinement which has gained significant interest in the study of fundamental physics in low-dimensional electron systems. In such semiconductor heterostructures, there are fundamentally three possible ways of band alignment: type-I (straddling gap), type-II (staggered), and type-III (broken gap)[41].

A type-I band alignment occurs at an interface between two materials with different bandgaps. In this scenario, the CB and VB of one semiconductor are higher and lower, respectively, than those of the other semiconductor, as illustrated in Fig 2.3(a). Electrons and holes tend to move from materials with a higher bandgap to those with a lower bandgap. This band alignment creates a potential barrier for both electrons and holes from the lower bandgap material. By sandwiching the low bandgap material between two high bandgap materials, it is possible to create potential wells for the charge carriers. Both electrons and holes can accumulate in the lower bandgap material. When a low bandgap material is sufficiently thin, restricting electron motion in at least one spatial dimension, such as in a nanostructure, a transformation occurs, turning the potential well into a quantum well (QW)[42]. This change happens when the confinement dimension approaches the scale of the particle's de Broglie wavelength of the electron. At this point, quantum effects start to dominate over the behavior of the particles. In this QW scenario, instead of the typical continuum of levels within the energy bands, electrons within the material become constrained to discrete quantum states. QWs are often referred to as "quasi-two-dimensional" structures. The term "quasi" is used to distinguish

them from perfect two-dimensional systems, where the wavefunction is entirely confined to a plane and has no extension beyond it. The probability of finding an electron can be expressed through a wavefunction. Analyzing the squared wavefunction allows for the assessment of the probability of finding the electron at a certain spatial position. If the QW layer becomes too thick, the quantum confinement gradually diminishes, and the material begins to exhibit its bulk properties, akin to a larger three-dimensional counterpart. Electrons and holes can still be confined to the potential well.

In the case of the type-II heterostructure, Fig 2.3(b), the band edges of one material are above the corresponding band edges of the other material, so the electrons tend to accumulate on one side of the heterojunction and the holes on the opposite side. In the type-III heterojunctions, the valence band edges of one material are above the conduction band edges of the other material shown in Fig 2.3(c). Electrons on one side of the heterointerface can go through it to the other side, from VB to CB. This type of heterointerface is sometimes referred to as a type-II heterojunction with a broken gap, or misaligned band structure.

Depending on the band alignment at the interface of semiconductors, when there is a disparity in the potential of the charge carriers, a transfer of charge carriers occurs between the two materials. This transfer continues until the Fermi levels on both sides align with each other. This phenomenon results in the band edges bending at the interface. On one side of the interface, the band edges incline upwards while on the other side, they tilt downwards, forming semi-triangular potential wells at each side of the heterojunction shown in Fig 2.11.

The crystalline nature of many semiconductors, characterized by a distinct three-dimensional lattice structure, introduces a potential challenge when two different semiconductor materials with different lattice arrangements are brought into contact at a heterointerface. This lattice mismatch can lead to mechanical strain and the creation of a substantial quantity of defects at the interface, thereby impacting the electronic band structure. In addition, undesired atomic intermixing and irregularities in the interface can arise, compromising the interface quality even further. These issues can have a significant adverse effect on the transport of charge carriers along the interface by causing scattering, thereby impairing the overall performance of the semiconductor device.

2.2.1 Polytypism

The previously mentioned challenges of interface roughness and atomic intermixing can be mitigated using a polytype heterostructure composed of the same materials with different crystal structures[43]. Prior to a detailed exploration of polytype heterostructures, it is essential to discuss the crystal structure of the materials. Most semiconductors are materials that have a crystalline structure and can crystallize in

various ways. The structure of a crystal can be seen to be composed of a repeated element in three dimensions. This repeated element is known as the unit cell. The shape and symmetry of their unit cells classify them into several fundamental crystal systems. Within a crystal, it is possible to identify planes of atoms that are equally spaced, and Miller indices is a notation system used to describe these crystal planes[34]. For example, in a three-axis system with equidistant vectors, the x direction is the [100] direction, while the z direction is the [001] direction. They are normal vector to planes described by the Miller indices being (100) and (001), respectively. Besides these directions, it is also possible to identify repeating planes at different angles, such as the [111] direction. The crystal orientation can also be defined using a four-axis system when this is more convenient e.g., for the hexagonal systems.

In this thesis, the optical properties of one III-V binary semiconductor, namely InP, are investigated. III-V semiconductors consist of atoms from group III and group V of the periodic table. The III-V bulk materials are usually arranged in the zb crystal structure, which is a combination of two face-centered cubic (FCC) crystal structures, one of which is translated by $1/4^{th}$ in all three directions. Despite having multiple atoms of different types in the unit cell, it is possible to construct a unit cell that is cubic with lattice constants a = b = c and angles of 90° between the axes of the unit cell as shown in Fig 2.4(a). The crystal structures that are similar to FCC, such as zb, are often called cubic close-packed (CCP) structures, as they are among the most optimal stacking sequences.

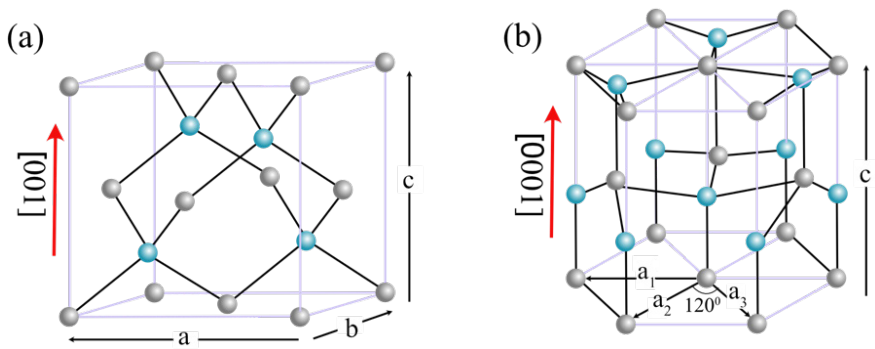

***Figure 2.4**: (a) The zb crystal unit cell. (b) The wz crystal structure unit cell.*

However, in some cases, the III-V binary semiconductor's closely related hexagonal counterpart, the wz structure, is found in bulk materials, e.g. when nitrogen is the group V component in III-V compounds. But generally, wz is not the stable crystal structure for non-nitride III-V bulk materials. The wz structure is hexagonal, with the angle between the lattice vectors a and b being 120°, and one translation vector being of a different length, a = b ≠ c. The wz structure is constructed from two

interpenetrating hexagonal close-packed (HCP) lattices. Generally, this structure is represented by a four-axis system with $a_1 = a_2 = a_3 \neq c$ and angles of 120° between $a_1 = a_2 = a_3$, and 90° between $a_{1,2,3}$ and c as shown in Fig 2.4(b). For bulk growth of non-nitride III-V semiconductors, the dominantly formed crystal structure is zb. However, for nanoscale structures, it is possible to grow nanostructures adopting the wz crystal structure for important semiconductors, such as GaAs, GaP, InAs, and InP. The possibility for materials that adapt different crystal structures characterized by a different arrangement of layered structural units (III-V bilayers in this case) is known as polytypism, and different crystal structures of the same material are called polytypes.

The atomic arrangement of the wz and zb crystal phases look quite similar along the [111] direction of zb, which is equivalent to the [0001] direction of wz shown in Fig 2.5[44]. Each subsequent layer has the same atomic arrangement, and they only differ in the arrangement of the stacking sequence of the layers themselves. The hexagonal wz nanostructure grows with In and P atoms stacked in an AaBbAaBbAaBb… stacking sequence. Here, each pair of letters such as Aa or Bb represents an atomic bilayer (for instance In and P) along the [0001] direction, and the period repeats every two bilayers shown in Fig 2.6(a). Each layer is rotated forward and backward by 60° in the plane with respect to the previous layer. In this stacking sequence, every third layer is oriented the same way.

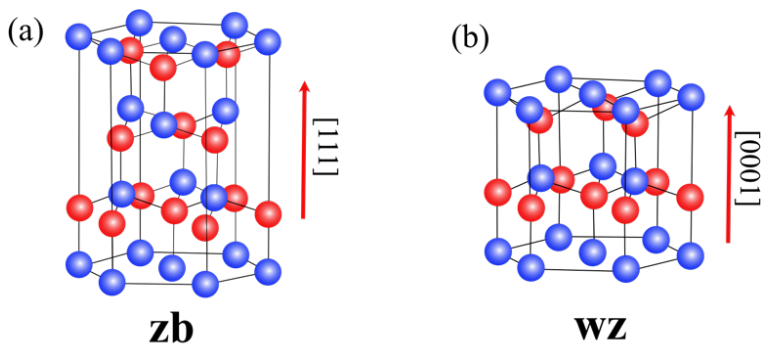

Figure 2.5: *The zb is presented in the direction [111] (b) The wz is presented in the direction [0001]. The arrows (red lines) are the growth directions.*

When the crystal grows on top of layer Bb, it can result in another stacking, different from the HCP one where layer Cc is formed instead of layer Aa in the wz structure. This causes the CCP zb crystal structure to form along the [111] direction. In this structure, In and P atoms are stacked in an AaBbCcAaBbCc… sequence, with the period repeating every 4th bilayer shown in Fig 2.6(b). Each bilayer is rotated by 60° with respect to the previous layer, and the orientation of the fourth layer is the same

as the first layer. To better visualize the stacking of the zb (FCC) and wz (HCP) crystal structure, Fig 2.6 shows the crystal structure along [111] (zb) direction and [0001] (wz) direction, where sets of two atoms are approximated with big spheres.

The $[\bar{1}\bar{1}\bar{1}]$ direction and $[000\bar{1}]$ directions are opposite to the [111] and [0001] directions, respectively, but they have the same layer orientation, however, due to polarity difference in the basic symmetry operations of the crystal symmetry, the $[\bar{1}\bar{1}\bar{1}]$ -equivalent directions are terminated by A-type atoms (P in the case of InP) while the opposite one [111]-equivalent is terminated by a-type atoms (In in the case of InP). Therefore, the $[\bar{1}\bar{1}\bar{1}]$ direction of zb is equivalent to the $[000\bar{1}]$ direction of wz.

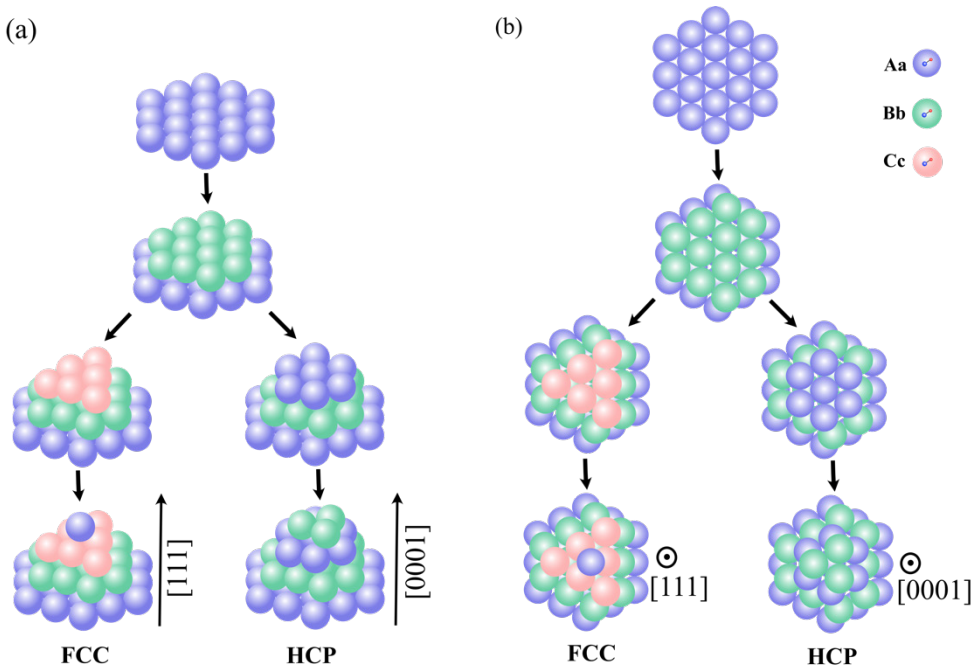

Figure 2.6: *Structural representation of the (a) zincblende (FCC) and (b) wurtzite (HCP) lattice. In the HCP lattice, the stacking sequence is AaBbAaBb..., while in the FCC lattice, it is AaBbCcAaBbCc…as shown in Fig 2.7. Here, Aa or Bb represents an atomic bilayer, such as In and P. Sets of two atoms of In and P together are depicted with large spheres for clarity. The color of the large sphere correlates with the color of the slab in Fig 2.7.*

These polytypes can be used to form heterojunctions similar to conventional heterojunctions but offer several advantages over the latter. One of the main benefits is the avoidance of strain that arises from lattice mismatch, interface roughness, and compositional intermixing. Since polytype heterojunctions consist of the same

compound, such as zb and wz InP, they create a sharp interface with no atom intermixing, minimal strain, and less surface roughness[43]. This is in contrast to conventional heterojunctions, where abrupt changes in material composition, such as InAlN/GaN[10], can lead to significant strain. On the other hand, one drawback of the polytype heterostructures is the limited variability in band gap energy variation compared to the compositional counterparts. With a lower and fixed band offset and a shallower potential well, the design range for quantization and hence emission energy within these systems is limited, which restricts the desired bandgap engineering. These polytype heterostructures are achieved by varying the crystal phase within a single nanoscale structure. The possibility of having wz and zb phases within a single nanostructure allows for a new direction for bandgap engineering[45].

2.2.2 Nanostructures

In this work, two distinct nanostructures of InP were investigated: NWs and platelets. NWs are quasi-one-dimensional structures with diameters ranging from 10 nm to 1 µm and lengths in the order of micrometers. We can achieve an engineered, polytypic heterostructure in NWs by creating a single interface between the zb and wz crystal phases, as shown in Fig 2.7. In NWs, the zb and wz grows predominantly in the $[\bar{1}\bar{1}\bar{1}]$ and $[000\bar{1}]$ directions, respectively[46].

In contrast, InP platelets are thin, two-dimensional structures made of InP crystal material. These platelets are typically grown using a process called selective area epitaxy, in which large-area InP wz layers (> 500 µm²) can be formed on top of zb InP substrates, as shown in Fig 2.8. InP platelets have a thickness in the range of a few tens to hundreds of nanometers, with lateral dimensions up to several micrometers[47]. In platelets, the zb and wz grow in the [111] and [0001] direction, respectively. This is the opposite direction (polarity) than for the NWs.

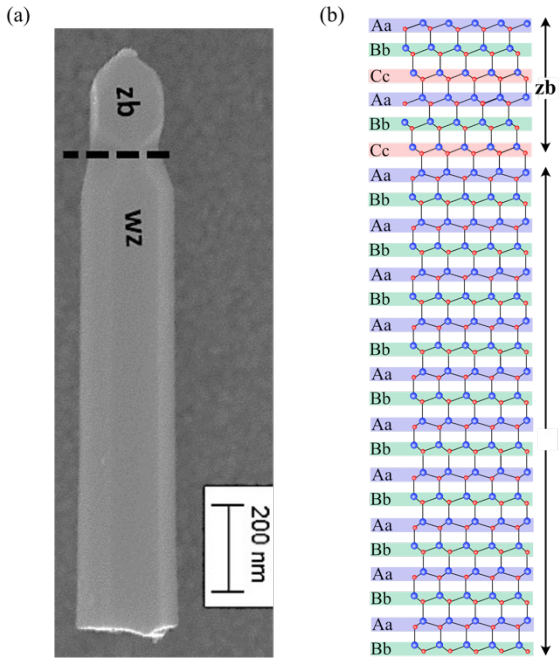

Figure 2.7: *(a) Scanning electron microscopy image of a wz/zb heterostructured NW, (b) zb (top), and wz (bottom) structures and their stacking sequence.*

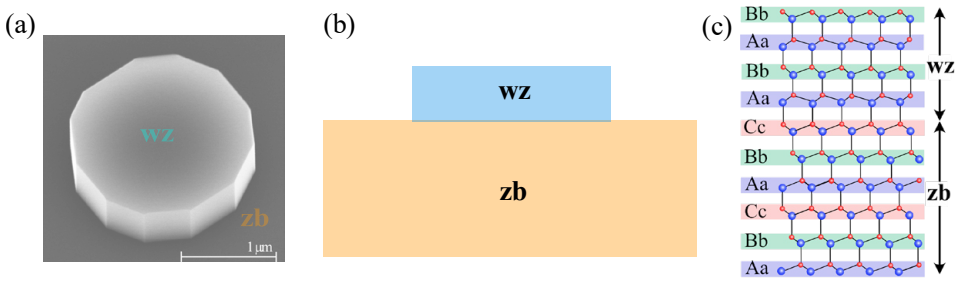

Figure 2.8: *(a) Scanning electron microscopy image of a platelet, (b) a schematic representation of wz (top) and zb (bottom) structures, and (c) their corresponding stacking sequence.*

2.3 Recombination Dynamics

External excitation introduces a charge carrier distribution that deviates from the thermal equilibrium state. In our context, this external excitation is achieved optically. The interaction between semiconductors and optical excitation with photon energy higher than the bandgap creates an optical transition of charge carriers, where electrons are promoted from the VB to the CB and leave holes behind in the VB. The optically generated electrons and holes thermalize rapidly (around 10^{-12} s) and relax to the lowest energy level available in the CB and highest energy level in the VB transferring the excess energy to the lattice, for instance through phonon interaction. The electrons in the CB can recombine with holes in the VB, leading to the emission of a photon with an energy corresponding to the bandgap. The emission of light after excitation is known as PL[48]. In addition, there are non-radiative recombination paths, not resulting in any photon emission. Unintentional impurities, defects, and intentional doping can also create energy levels within the bandgap leading to new paths for charge carrier recombination. The recombination associated with these paths is represented by the green arrows in Fig 2.9. Only radiative recombination is considered here. These recombination paths lead to the emission of a photon with an energy lower than the bandgap. The emission energy of the exciton recombination is lower in energy than the bandgap energy due to the binding energy of the electron and hole. The recombination associated with an exciton is represented by the blue arrow in Fig 2.9.

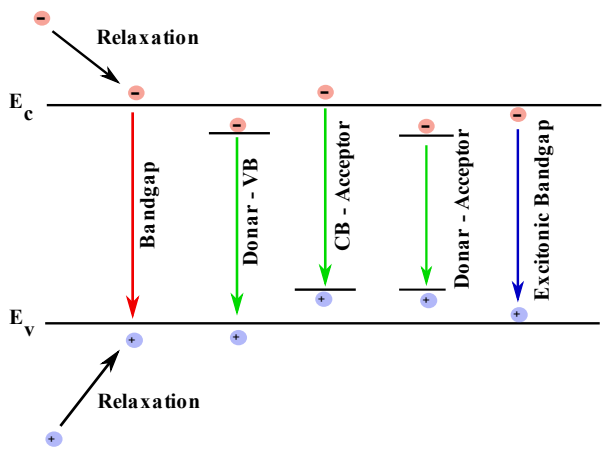

Figure 2.9: *Radiative PL processes. Red: the band-to-band recombination. Green: the recombination involving energy levels within the bandgap. Blue: recombination associated with the formation of an exciton*

Electron energy levels can be characterized by a wavefunction distribution. When an electron wavefunction in the CB and a hole wavefunction in the VB overlap spatially, it can lead to recombination and the emission of a photon. In direct bandgap semiconductors, this overlap occurs extensively because the CB minimum and VB maximum are situated at the same point within the Brillouin zone, both in terms of reciprocal and real space. However, in the case of materials with a direct bandgap, the large overlap between the electron-hole wavefunction leads to a fast recombination rate and a short recombination time for the charge carriers. The overlap is also constant with time after pulse excitation and the recombination rate generally does not depend on the time after the pulse as shown in Fig 2.10 for wz recombination. The time it takes for the emission intensity to decay to 1/e (37%) of its maximum concentration is referred to as the lifetime[49].

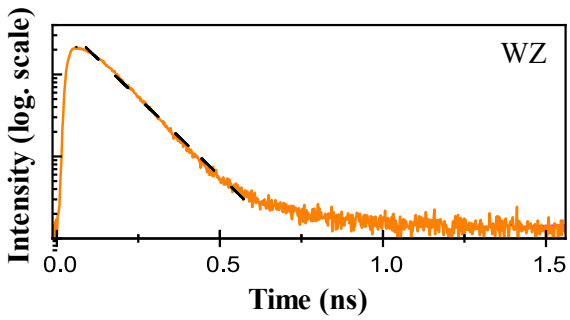

Figure 2.10: *Time-decay of the PL intensity of the wz emission shows an exponential PL decay. The black dashed straight line in the semi-log plot denotes the time-independent recombination rate.*

The recombination dynamic is quite different for charge carriers at the type-II interface. At the type-II interfaces, band bending creates triangular potential wells on the opposing side of the interface, as discussed earlier. Recombination across such a heterojunction is possible, even though the photogenerated charge carriers are accumulated at the spatially separated potential wells at the interface[50]. Spatially separated charge carriers bound by the Coulomb force create IXs. They are indirect in real space and form dipoles perpendicular to the interface. As shown in Fig 2.13(b) the wavefunctions of charge carriers penetrate through the barrier due to the abruptness of the interface and the resulting partial overlap of the wavefunctions of charge carriers from both sides of the interface causes IXs recombination. We define the emission at the type-II interface as IX emission. In our study, the excitation energy is above the bandgap energy of both wz and zb InP, and the photogenerated charge carriers lose their excess energy when relaxing to the band-edge of their respective band. These charge carriers can either recombine in the wz and zb segments of InP, or they can diffuse to the interface as shown in Fig 2.11. The

electrons will accumulate in the conduction band of the zb InP and the holes will accumulate in the VB of the wz InP.

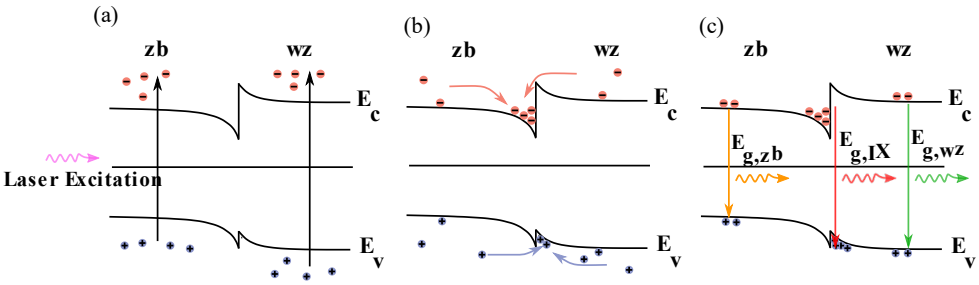

Figure 2.11: *(a) Photogeneration of electrons and holes through laser excitation. (b) Relaxation and diffusion of electrons and holes. (c) Recombination of electrons and holes.*

The accumulation of charge carriers in the potential well can be affected by the EPD of the laser. At higher EPD, the potential well is filled with charge carriers as shown in Fig 2.12(a) upper panel and recombination takes place from all energy levels in the potential well. The recombination rate is the probability of recombination of an electron-hole pair. The recombination rate for charge carriers between two interband energy levels (from CB to VB) is proportional to the squared integral of the overlap between the electron-hole wavefunctions of those interband energy levels[23]. So, the recombination rate of the IX emission is given by the overlap of the parts of the wavefunctions that penetrate the barrier. Assuming that the penetration of the wavefunctions through the barrier for a higher energy level is larger than for the wavefunctions of the lower energy level due to the additional kinetic energy, the dominant recombination takes place from the highest occupied energy level. Even though the emission at a low energy level is present at a high EPD, the emission is dominated by the high-energy emission due to the larger overlap of wavefunctions, resulting in a higher recombination rate. The normalized plot in Fig. 2.12(b) illustrates that the spectra for high EPD exhibit an emission peak at high energy. However, there are also tails extending to low energy. With low EPD and a low number of excited charge carriers, only a few charge carriers occupy the lowest energy levels of the potential wells as shown in Fig 2.12(a) lower panel. As a result, recombination only takes place from lower energy levels. IX emission occurs at an energy below the bandgap of the semiconductors in the structure at a very low EPD. This leads to an apparent redshift of the emission energy with decreasing EPD as shown in Fig 2.12(b) It is important to note that we assumed that the slope of the potential well, as discussed in this context, remains relatively unchanged with variations in charge carrier density which is induced by changes in laser EPD.

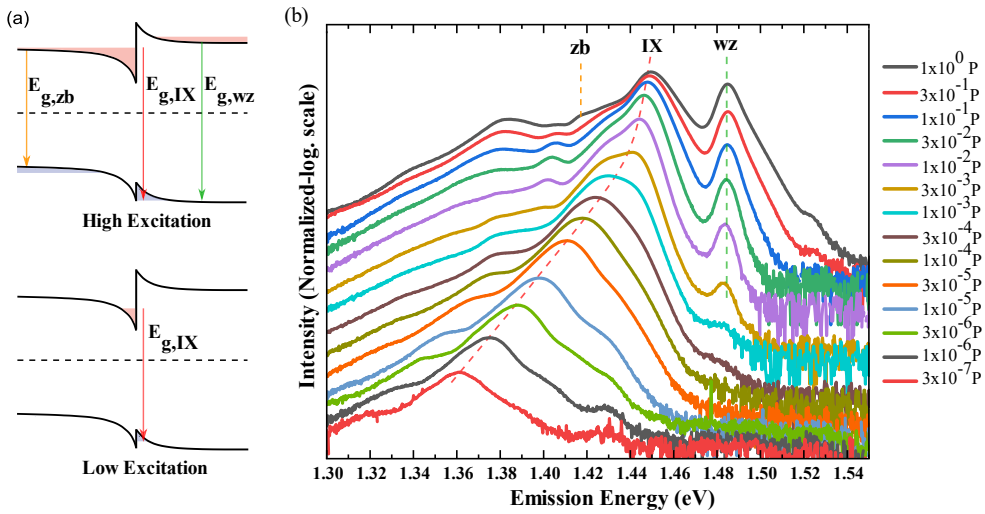

Figure 2.12: (a) *The spatially indirect recombination across a wz/zb InP interface at high and low EPD. (b) power-dependent PL spectra of an undoped single wz–zb InP platelet as a function of EPD.*

For the type-II interface, the spatial separation of charge carriers plays a crucial role in the recombination dynamics. First, it creates a longer recombination time as only a fraction (or part) of the electron-hole wavefunctions overlap through the barrier resulting in a slow recombination rate. It results in significant emission even 30 ns after excitation, as shown in Fig 2.13. Second, in the case of IX emission, the recombination rate becomes time dependent. To elaborate in more detail, immediately after the excitation pulse, the transition between the highest occupied energy levels dominates the emission in the decay profile because the penetration of the wavefunctions through the barrier for these levels is larger than for the wavefunctions of the lower energy levels. In addition, this leads to a faster recombination rate which causes the steeper slope in the initial part of the decay profile in Fig 2.13. Those higher energy levels gradually deplete with time due to recombination, the overlap of the wavefunctions is reduced, and the recombination rate slows down with time which results in the dominating emission to shift down in energy. The varying recombination rate leads to the observed non-exponential decay profile. It is not possible to fit the decay profile with a single exponential function. We therefore cannot define the term ´lifetime´ for the IX emission.

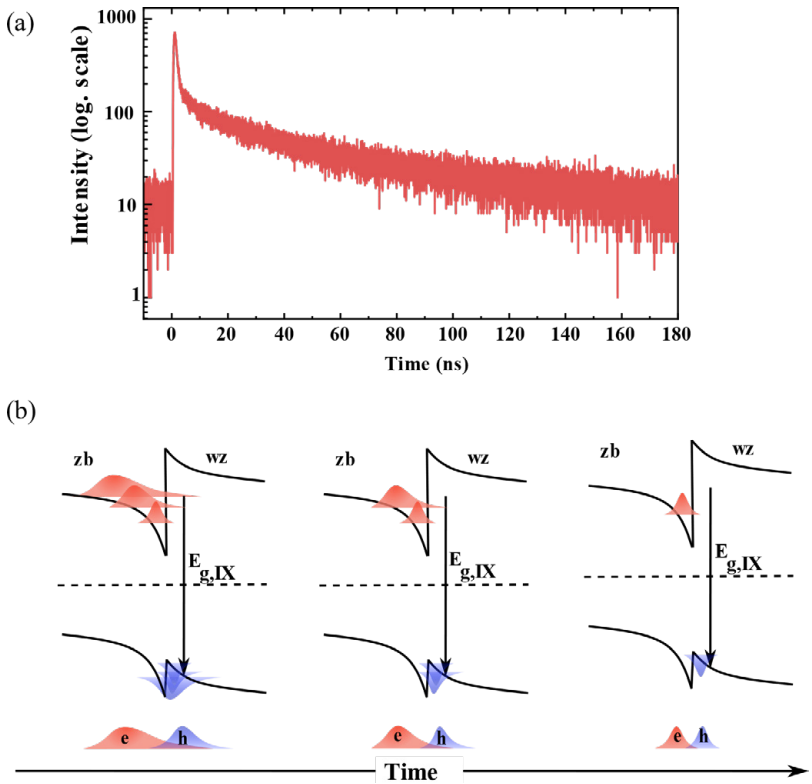

Figure 2.13: *The time-dependent decay of PL intensity of the IX emission of an undoped wz/zb NW (a) shows a nonexponential PL decay profile in log scale. (b) A schematic explanation for the temporal evolution of overlapping of the wavefunctions for holes and electrons at the interface. Directly after the pulse excitation, the overlap of the wavefunctions is high since there are charge carriers available in high energy levels, whereas at later times only charge carriers with lower energy levels are available. These charge carriers have a smaller overlap of the wavefunctions.*

At room temperature, the potential well is typically fully occupied with thermally generated charge carriers, making the observation of the IX emission challenging. Emissions from wz and zb structures are more prominent under these conditions. To observe the IX emission, a lower temperature is required, where the potential well does not contain thermal carriers. Only optical excitation can fill the potential well in this scenario.

At low temperature, it is possible to have charge carriers in the potential well without optical excitation. For instance, the CB can be filled with electrons if a 2DEG forms within it. The formation of a 2DEG can be achieved through modulation doping in the wz segment of a heterostructure[51]. The concept of a 2DEG pertains to a system in which electrons are constrained to move within two dimensions, often occurring at the interface between two semiconductor materials. As a result, the motion of electrons becomes effectively confined to the two

dimensions of the potential well in the CB at the type-II interface. In this modulation-doped structure, dopant atoms are intentionally positioned away from the type-II surface, minimizing charge carrier scattering from dopants. Due to the modulation doping in the wz region, electrons are naturally present in the CB at the type-II interface, even at the low temperatures.

2.4 Indirect Exciton Transport

IXs can travel significant distances from the excitation spot, benefiting from their slow recombination rate that allows them to cover longer distances before recombination. The transport regime for IXs is divided into two distinct modes:

1. **Diffusive:** At low EPD, IXs travel comparatively shorter distances from the excitation spot before recombining, primarily driven by diffusion along concentration gradients away from the excitation spot.
2. **Repulsive Force Drive:** At high EPD, the spatial spread of IX emission significantly expands compared to lower EPD. This suggests a transition in the transport of IXs from a diffusive to a driven mode. The driving force behind this expansion is the Coulomb repulsion between aligned IX dipoles. At high EPD, there is a high concentration of IXs at the type-II interface, causing the aligned IX dipoles to repel each other. This repulsive force becomes dominant over diffusion, facilitating the longer-distance transport of IXs.

Regarding the spatial expansion with time of IXs, immediately after the laser pulse, the IXs undergo rapid expansion, and as time progresses, the behavior becomes linear. This initial period is attributed to the high IXs density following the pulse, resulting in repulsive interactions between aligned IX dipoles. These repulsive forces cause the IXs to quickly move away from the excitation spot initially. As time elapses and the density of IXs decreases, the diffusion properties of IXs become dominant.

3 Experimental Methods

In this section, we elucidate the experimental methodologies employed in the present study. Each paper within this thesis centers on the creation of InP nanostructures, along with optical spectroscopic examinations conducted through steady-state photoluminescence (SSPL) spectroscopy and time-resolved PL spectroscopy (TRPL). Additionally, both optical and electron microscopy are employed for the morphological analysis of the nanostructures. Finally, comprehensive insights into sample preparation are provided.

3.1 Growth

A wide range of growth techniques can be utilized for the fabrication of nanostructures, with metalorganic vapor phase epitaxy (MOVPE) being a commonly employed method[52]. MOVPE enables the epitaxial growth of semiconductor crystals from vapor phase precursors. The term "epitaxial" refers to the ordered growth of a crystalline structure on a crystalline substrate. This process involves depositing additional crystalline layers on a seed crystal or substrate, which serves as the foundation for the growth. MOVPE relies on the transition of material from a vapor phase to a crystalline phase. For III-V semiconductors such as GaAs, InP, or GaSb, commonly metal-organic precursors containing group III elements as well as group V hydrides are introduced in the gas phase. For the specific case of InP, these precursors are trimethylindium (TMIn) for the group III atoms and phosphine (PH_3) for the group V atoms. In addition to the zb crystal structure that is stable in III-V bulk material, nanostructures can also be grown in the wz crystal structure. Compositional heterostructures can be grown by switching the precursors, for instance from InP to GaInAs[52]. On the other hand, homomaterial, polytype heterostructures such as wz/zb InP can be achieved by adjusting growth parameters such as temperature and/or the molar fractions of the precursors[43,53-55]. Doping of NW structures can be achieved by introducing dopant precursors during the growth process. Doping can also be used to control the resulting crystal structure[56-58]. This means that intentional doping can modify the crystal structure.

In our experiments, we have investigated two types of MOVPE-grown nanostructures, both types including wz/zb heterostructures: NWs and platelets. For NW growth, the VLS mechanism is a prevalent approach, involving a liquid phase

particle in most cases to facilitate crystallization. While effective for NWs with nanometer-scale diameters, this mechanism may not be suitable for larger diameter nanostructures or structures in the micrometer range. In such cases, catalyst-free selective-area growth is an alternative method that enables the growth of larger area InP platelets.

1. For NW synthesis, a commonly preferred approach is the use of Au particle-assisted growth using the vapor-liquid-solid (VLS) growth mechanism[59]. The use of a seed particle facilitates vertical growth control, including NW diameter, and can promote the formation of axial heterostructures. To complement the picture, radial heterostructures can also be formed. This exclusively includes compositional and not polytypic heterostructures. The radial layers tend to adopt the crystal structure of the core.
2. In contrast to the NW architectures, a particle-free growth method is employed for our platelet structures, the selective area growth (SAG). This technique relies on growth selectivity triggered by a pre-patterning of the growth substrate, where a mask prevents the growth on the substrate except in the selected pattern areas. The lateral size of the structures can be made much larger than for the NW approach. The polytypic interface forms between the zb growth substrate and the growing wz platelet (film)[60,61].

3.1.1 Particle-Assisted Nanowire Growth

The growth of highly anisotropic crystals in the shape of NW structures is achieved using metal nanoparticles as growth catalysts through the VLS growth method[59]. In this method, metallic seed particles, typically Au, are deposited onto an InP $(\bar{1}\bar{1}\bar{1})$B substrate. Fig 3.1 shows a schematic of the particle seeded VLS growth method. The substrate is heated in a reducing atmosphere (predominantly hydrogen) to remove residual oxides. Group III and V precursors are introduced in the gas phase to facilitate the growth of III-V NWs on the substrate. The Au particles absorb mostly the group III-element material and form a liquid alloy droplet. When the group III and group V material concentration in the liquid alloy droplet becomes supersaturated, meaning it exceeds the equilibrium concentration, the growth of the NWs starts. The subsequent growth of NWs occurs layer by layer beneath the Au alloy particle in the axial direction. Lateral (radial) growth, also referred to as shell growth takes place on the sidewalls of the NWs following the vapor-solid (VS) growth mechanism. This has a significantly slower rate compared with the axial growth at conditions optimized for axial NW growth. The shell grown during radial overgrowth has in most cases an epitaxial relationship with the core, meaning it adopts the same crystal structure. For the final structure, the diameter of the axially grown NWs is predominantly determined by the size of the deposited catalyst particle, while the length is determined by conditions such as growth time, material supply, and growth temperature. The growth conditions can be modified to promote

radial growth and create radial heterostructures as well, such as controlled core-shell heterostructures. This can typically be achieved by, for instance, increasing the growth temperature or varying the nominal V/III ratio of the precursor fluxes.

In our study, randomly distributed aerosol particles with an areal density of about 1 μm^{-2} were used as seeds for the NW growth. Au particles with a diameter of approximately 30 nm were dispersed as growth catalysts, resulting in the growth of pure wz NWs with an average length of 2 µm. By further modifying the growth conditions, a single zb top segment with a length of about 200 nm was added on the top of the wz structure. This was achieved by altering the group V hydride flow. The transition region between wz and zb segments exhibited superior crystal quality meaning an atomically sharp switch between the two crystal phases without structural defects such as stacking defects, interface roughness, or atomic intermixing[22,53]. For doped polytype InP NWs, hydrogen sulfide (H_2S) was introduced as a dopant during the growth of the wz segment, resulting in an n-type doping concentration of approximately 10^{20} cm^{-3} [56]. For more detailed information on the NW growth processes studied in our work, please refer to the provided reference[43].

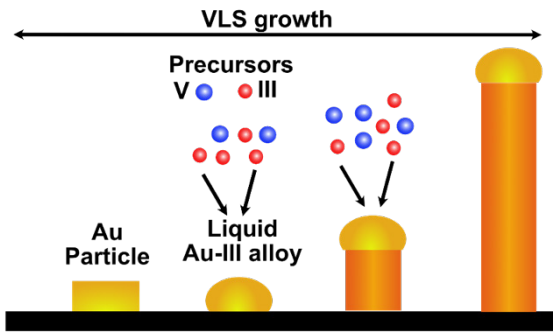

Figure 3.1. *Schematic illustration of the sequential phases of VLS growth. Initially, Au particles assimilate precursor gas elements, typically under elevated temperatures. Subsequently, a nucleation step occurs. The third stage marks the commencement of actual NW growth, followed by the fourth stage representing the fully grown NW.*

3.1.2 Selective Area Platelet Growth

Selective area growth is a technique utilized to promote epitaxial growth in specific regions of a single crystalline substrate by utilizing an inert mask template. In the case of growing InP platelets, the process involves initially depositing a layer of silicon nitride (SiN_x) onto an InP (111)A wafer substrate using plasma-enhanced chemical vapor deposition. Subsequently, circular openings are created in the SiN_x films using UV-lithography, followed by wet-chemical etching and an oxygen plasma treatment. The latter is to clean the surface before growth. Following these steps, the substrates are placed into the MOVPE growth chamber. The growth process is initiated by preheating the sample and subjecting it to annealing in a PH_3/H_2 atmosphere. The temperature is then increased to the desired growth temperature for thermal stabilization followed by the introduction of III and V precursor gases to trigger the growth process. The circular openings in the mask are arranged in a hexagonal pattern with a diameter-dependent pitch value, while the diameter of these openings, referred to as d_0, ranges from approximately 2 to 28 µm. With a growth time of 10 minutes, we were able to achieve a thickness of approximately 400 nm of wz on the zb substrate. Fig 3.2 shows the SAE grown platelets. For a more comprehensive understanding of the platelet growth studied in this work, additional information can be found in the provided reference[47].

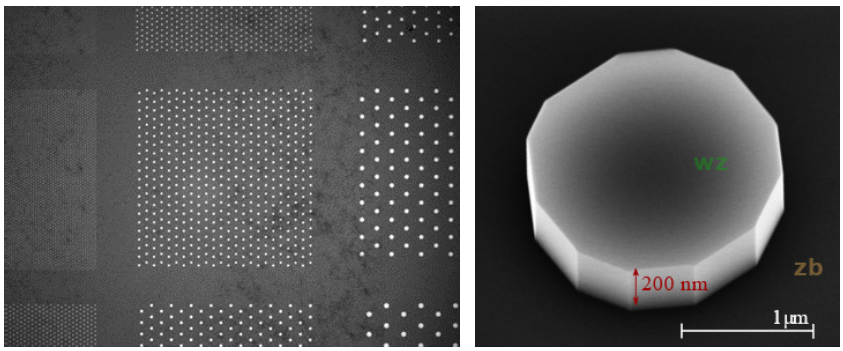

Figure 3.2. *(a) An optical microscopy image of platelet arrays exhibiting varied diameters, ranging from a smaller size of 2 µm (top left) to a larger one of 28 µm (bottom right). Additionally, (b) Scanning electron microscopic image depicting a single, representative platelet with a nominal diameter of 2 µm recorded with a 30° tilt.*

3.2 Photoluminescence Spectroscopy

In this study, PL spectroscopy, a non-intrusive method, is utilized to investigate the optical properties of engineered, polytypic InP nanostructures. The focus has been on two specific techniques: SSPL and TRPL spectroscopy. PL spectroscopy is a rapid technique that only requires a relatively straightforward optical setup, making it suitable for scientific research and as a means of obtaining quick feedback on the structures under investigation[25]. With the ability to vary the excitation energy (or wavelength) and power over large ranges, it is a technique that is very suitable for studying dynamic processes in semiconductors. The schematics of the setups employed in this work are shown in Figs. 3.3 - 3.5, and a detailed description will follow in the subsequent sections. First, some common features associated with the specific techniques applied in this study will be discussed. Excitation and detection are integral components of PL spectroscopy. To initiate the process, charge carriers are excited across the bandgap using a high-energy light source such as a laser. Subsequently, the generated charge carriers recombine, resulting in the emission of a photon with a corresponding energy that can be detected and analyzed. To study the EPD-dependent PL emission, it is necessary to be able to vary the laser power. The effects and importance of varying the EPD were described in the introduction. Practically this can be done by altering the driving current of the laser. However, this can result in laser emission instabilities. Therefore, we followed an alternative approach and maintained a fixed power output of the laser while using a variable neutral density (ND) filter to achieve a variable EPD. In some cases, different excitation wavelengths are needed for the experiments and therefore a tunable laser is employed. As described in chapter 2, it is beneficial to perform the investigations at low temperature. To conduct these low-temperature measurements, the sample is placed in a cryostat that is cooled using liquid helium. This cryostat is positioned on a translational stage, enabling precise positioning and measurement of specific single nanostructures.

The sample is illuminated through the objective lens using a 50/50 beam-splitter, with 50% of the laser light directed onto the sample and another 50% of the laser light directed to a power meter for measuring the laser power. After the excitation of the sample, the very same objective lens and beam splitter collects the emitted light, including luminescence from the sample and the reflected laser line. This technique is known as the backscatter or confocal mode. The beam splitter directs 50% of the collected light from the sample to the detection system. In cases where the laser power output is lower and thus the 50% of the laser light directed onto the sample is too low to generate sufficient intensity of the emission of interest, a dichroic mirror can be used instead of a beam-splitter. The dichroic mirror selectively allows certain wavelengths to transmit through while reflecting others. It serves the purpose of allowing only emission from the sample to pass while blocking the reflected laser light. Therefore, it effectively enables nearly 100% of

the incident laser light to reach the sample and allows the collection of luminescence, with almost 100% transmission for detection. The choice of objective lens and hence the magnification power depends on the specific measurement requirements. For PL measurements, a 20X objective lens with a numerical aperture (NA) of 0.45 is utilized. This magnification power is sufficient for localizing individual nanostructures and collecting emissions from these structures. However, for spatially resolved PL measurements, a higher magnification of 40X having an NA of 0.60 is employed to enhance the spatial resolution.

The collected light is directed towards a spectrometer. In our experiments, the laser excitation energy (wavelength) is set above the bandgap of the materials, resulting in emitted wavelengths longer than the excitation laser wavelength. To selectively detect only the emission wavelengths, either a long-pass filter or a dichroic mirror is used. The collected light is focused onto the entrance slit of the spectrometer using a lens, and the PL is dispersed over the full width of a detector. Gratings with groove densities ranging from 300 to 1800 grooves/mm can be selected based on the desired spectral resolutions (for 300 grooves/mm the spectral resolution is around 0.16 nm/pixel). The dispersed spectrum of the emission is then detected using a thermoelectrically cooled charge-coupled device (CCD). CCDs are typically silicon-based integrated circuits featuring a densely packed matrix of photodiodes. These photodiodes function by converting the energy carried by incoming light, in the form of photons, into an electric charge. The magnitude of this charge is directly proportional to the intensity of the light captured by the respective pixel. This fundamental process enables the CCD to read and record visual information.

3.2.1 Steady-State Photoluminescence Spectroscopy

Fig 3.3 depicts a typical setup for SSPL spectroscopy used in this study. In this setup, a tunable titanium sapphire (Ti:Sa) laser with a continuous wave (CW) output is employed for excitation. The laser offers a tunable range of 705 nm to 880 nm, allowing flexibility in selecting the excitation wavelength. For our specific experiment, the excitation wavelength is typically chosen to be around 725 nm. This wavelength was chosen because it is above the bandgap of the samples used in the experiments. Additionally, the reflected laser wavelength from samples can be efficiently blocked by the longpass filter employed in the setup.

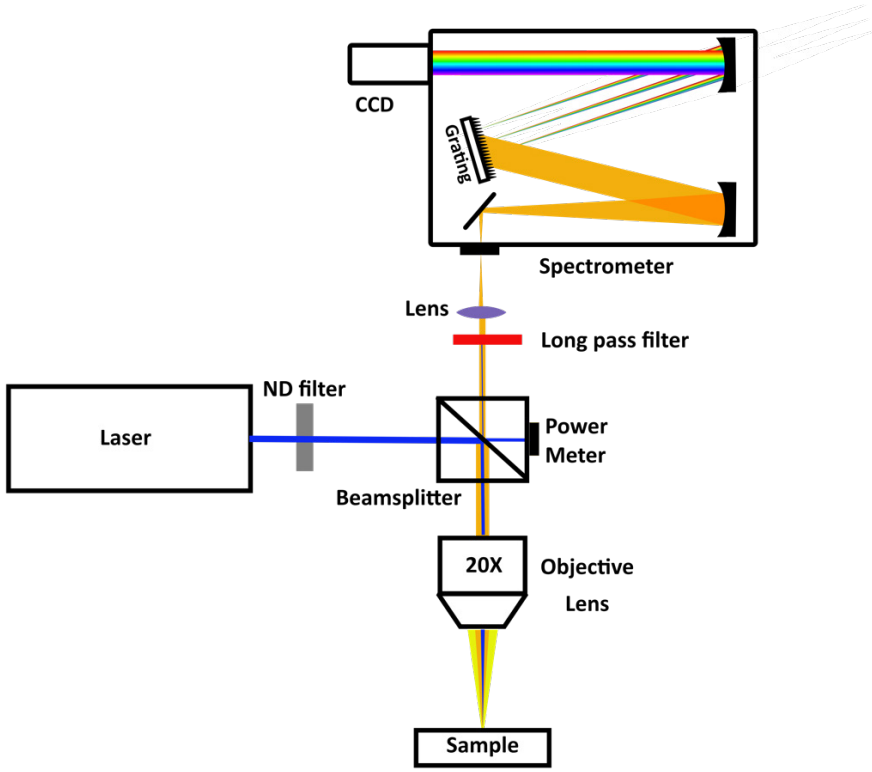

Figure 3.3. *A simplified schematic sketch of the PL setup used in this work. See text for a description.*

3.2.2 Time-resolved Photoluminescence Spectroscopy

TRPL is employed to analyze the recombination mechanisms of charge carriers following pulsed excitation[48]. The key distinction between TRPL and SSPL lies in the excitation source: TRPL employs a pulsed laser, while SSPL uses a CW laser. Furthermore, the detector used in TRPL measures the time-dependent change in PL intensity in response to the pulsed laser excitation, whereas SSPL detection is time-integrated. In TRPL experiments, a transient density of electrons and holes (e-h) is induced by the pulsed laser excitation, and the excess charge carriers undergo relaxation and recombination processes to reach equilibrium. The rise time of the emission trace primarily reflects the relaxation process of the generated charge carriers, while the decay of the emission corresponds to charge carrier recombination processes. This thesis employs three distinctly different setups for time-resolved photoluminescence, each of which with its own unique configuration and characteristics. The details and merits will be described in detail below.

3.2.2.1 Time-correlated single-photon counting

The principle of Time-Correlated Single Photon Counting (TCSPC) involves measuring the time delay between an exciting laser pulse and the arrival of an emitted photon at the detector[62]. In TCSPC, an avalanche photodiode (APD) is commonly used for photon detection. The APD with a single detection channel generally does not provide any spectrally resolved results. TCSPC is internally synchronized with the laser. In other words, the laser driver produces an electrical pulse that triggers the laser pulse, and the same electrical signal is the start signal for the counting module. The measurement necessitates a designated "start" signal supplied by the laser system and a specified "stop" signal attained through detection by the APD. This measurement is repeated for multiple periods, and the number of photons detected at specific delays after the pulse is recorded in a histogram, generating a time trace of the emission decay. Fig 3.4 illustrates the TCSPC setup for TRPL used in this thesis.

In this setup, a pulsed excitation source with a fixed wavelength of a 485 nm diode laser is employed. The repetition rate (frequency) of the laser pulses, set at 5 MHz is chosen based on the temporal behavior of the emission under study. This ensures that no emission remains from the previous pulse, while a higher frequency results in a shorter recording time. The light collected by the objective lens passes through a lens, creating an image plane where a slit with a variable width is placed to allow cropping of the image generated by the objective. The luminescence emitted from the sample is split by a 50/50 beam-splitter. One part is dispersed by a transmission grating and detected by a CCD for recording spectra, while the other part is directed towards an APD through a focusing lens to record the temporal behavior of the emission. Since the detection at the APD is not spectrally resolved, a spectral filter can be employed to select a specific wavelength. After receiving time-integrated spectrally resolved data at the CCD, we use the spectral filter to ensure the detection

of the desired spectral wavelength by observing the change in emission spectra at the CCD. Once the desired emission wavelength is ensured, we can detect the temporal behavior of the specific wavelength of emission.

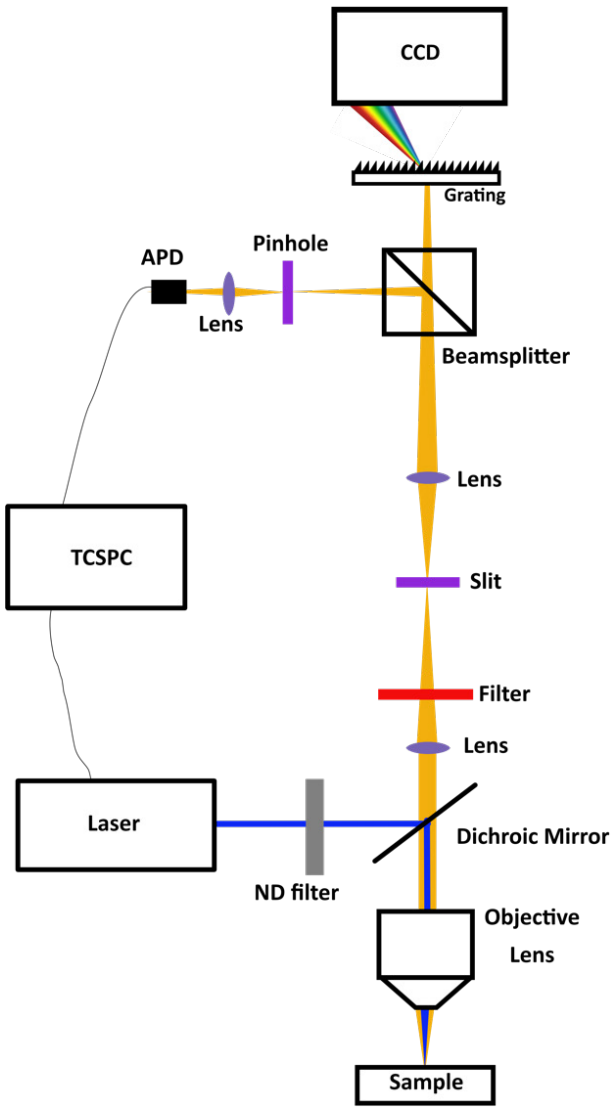

Figure 3.4. *A simplified schematic sketch of the TRPL setup with TCSPC used in this work. See the text for a detailed description.*

3.2.2.2 Streak Systems

In a streak system, it is possible to record temporal and spectrally resolved data by using either a streak camera or a streak scope, depending on the time scale of the phenomenon being studied. Both systems operate based on the same fundamental principles but are specifically designed for different time scales. For short time scales equal to or less than 2 ns, the streak camera is employed as the detection instrument. On the other hand, for longer time scales greater than 2 ns, the streak scope is utilized. These systems allow for the measurement of PL dynamics as a function of both wavelength and time simultaneously.

The main function of a streak camera or streak scope is to convert the temporal dependence of an optical signal into a spatial profile, which is recorded using a camera[26]. This conversion process allows for the visualization and analysis of the temporal dynamics of the optical signal. This is done by the following processes.

- Conversion of photons to photoelectrons:
  The process of converting photons to photoelectrons begins with the photons emitted from the sample being directed towards a photocathode (PC) by a spectrometer grating. The diffraction by the grating spreads the emission horizontally, identical to the description of the CW setup. The photoelectric effect takes place at the photocathode, where photoelectrons are generated upon absorption of the photons. These photoelectrons are then accelerated by an electric field.

- Deflection of the photoelectrons:
  The photoelectrons are deflected in the vertical direction by a time-dependent electric field, synchronized with the pulses from the laser. In the case of a streak camera, a sinusoidal voltage is applied to the deflection plates. The deflection results in a high-speed sweep, where early-time photoelectrons appear at the top and delayed photoelectrons appear lower down on the screen. The horizontal displacement corresponds to the wavelength of the photons, while the vertical displacement represents different time intervals with respect to the pulse. For the streak scope, a ramp voltage is used instead of a sinusoidal voltage on the deflection plates. This ramp voltage achieves a similar effect of displacing the photoelectrons vertically, but generally with a slower scan speed.

- Detection of the transverse position of the photoelectrons:
  Following the deflection plates, the photoelectrons pass through a microchannel plate (MCP) where they undergo amplification (typically about 10^3). The MCP acts as a high-gain amplifier for the photoelectrons. After the MCP, an image of the photoelectron distribution is generated. The amplified distribution of photoelectrons then strikes a phosphor screen, where the photoelectrons are converted into photons. These emitted photons are captured and recorded by a digital CCD camera for further analysis and visualization.

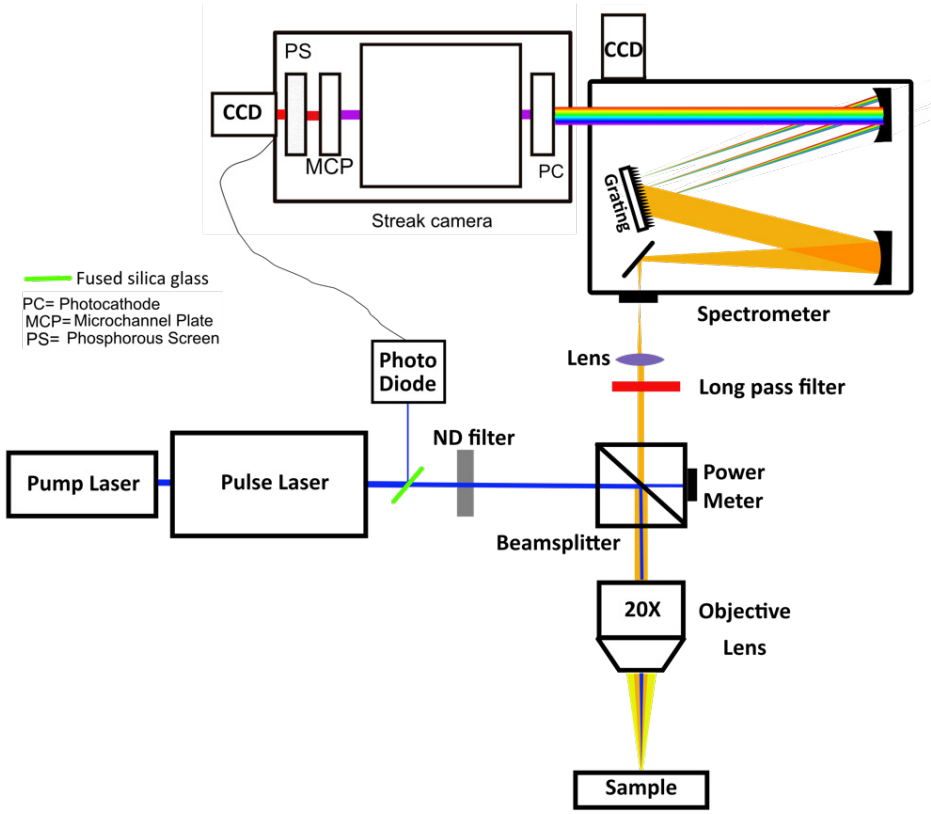

Figure 3.5: *Experimental setup for TRPL with a streak camera. See the text for a detailed description.*

A typical setup for TRPL using a streak camera is shown in Fig 3.5. In this setup, a pulsed Ti:Sa laser with a wavelength of 760 nm, pumped by a neodymium-doped yttrium aluminum garnet (Nd:YAG) laser, is used. The laser operates in pulse-mode locking, providing a pulse width of 62 fs, and a repetition rate of 81.8 MHz. A fused silica glass is utilized to redirect a small portion of the laser intensity toward a photodiode. Consequently, the photodiode triggers the streak camera for synchronization with the pulse of the laser. The temporal resolution of the streak scope is around 500 fs.

The principal setup for the streak scope is similar to the streak camera. For the streak scope setup, a pulsed laser with a wavelength of 653 nm and a pulse duration of approximately 39 ps is employed. The pulse rate can be varied within the range of 2 ns to 10 µs. In this case, a electronic trigger is simultaneously provided to both the laser and the streak scope. The shortest achievable temporal resolution of the streak scope is around 15 ps.

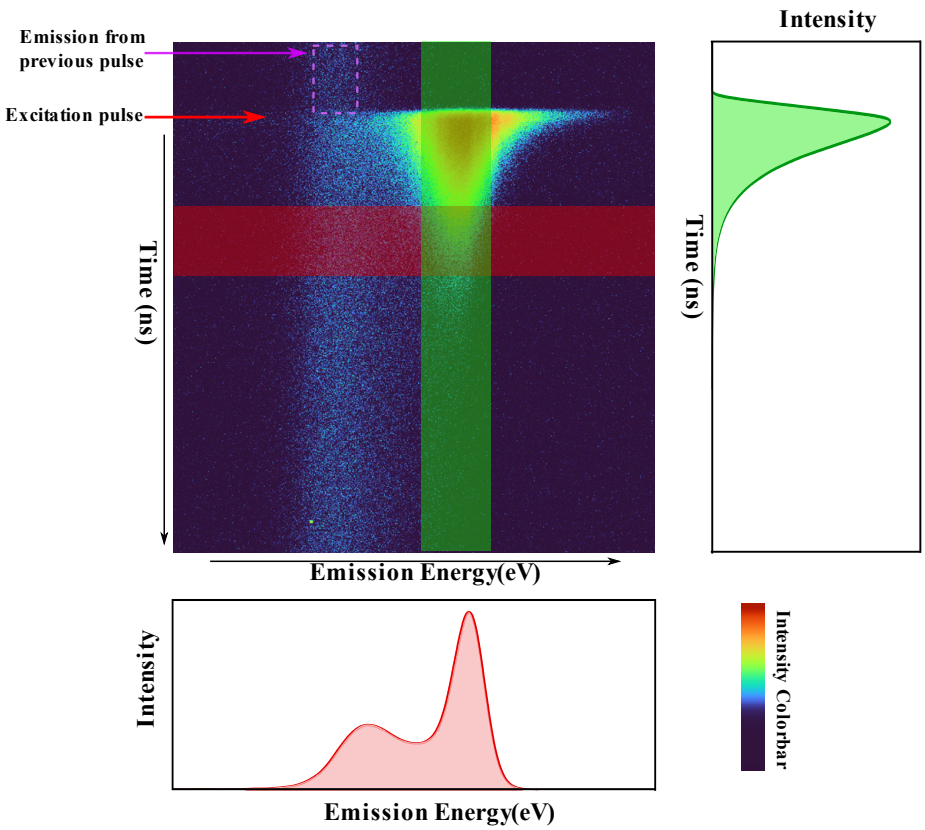

Figure 3.6: *A sketch of an example of a false color PL image recorded by a streak camera: The PL spectra and time trace are extracted from the 3D image by the integration of temporal (right) and spectral intervals (below), respectively.*

An example of a streak image is shown in Fig 3.6. The intensity of the PL signal is plotted as a function of photon energy on the x-axis and time on the y-axis in a false-color intensity scale. PL spectra can be extracted from horizontal cuts of the 3D image. This is done by integrating over a time interval, as shown in Fig 3.6. In the same way, from vertical cuts, time-dependent PL traces can be obtained by spectral integration, as shown in Fig 3.6. The arrival of the excitation pulse is defined by the upper boundary of the measured PL signal on top of the image at time zero. A weak signal coming from the previous excitation pulse at negative times can be seen if the lifetime is longer than that pulse spacing.

3.3 Local & Spatial Detection

Emissions can be detected through various methods. Local detection is employed when the detection spot coincides with the excitation spot, which is particularly useful for investigating the spectral features of emissions. This approach allows for a detailed examination of the spectral characteristics of emitted light from the detection point. Conversely, when a comprehensive analysis of the spatial characteristics of the emission is required, spatial detection is utilized. In this method, the detection area extends well beyond the excitation spot, enabling a broader perspective on the distribution and patterns of emitted light across a larger region. The key feature is that the light collection system projects an image of the sample under study on the entrance slit of the spectrometer. If the spectrometer is set to 0^{th} order, an image of the sample can be recorded by the CCD. By inserting vertical and horizontal slits, different modes of detection can be accessed, as described below.

3.3.1 Steady-state Photoluminescence Spectroscopy

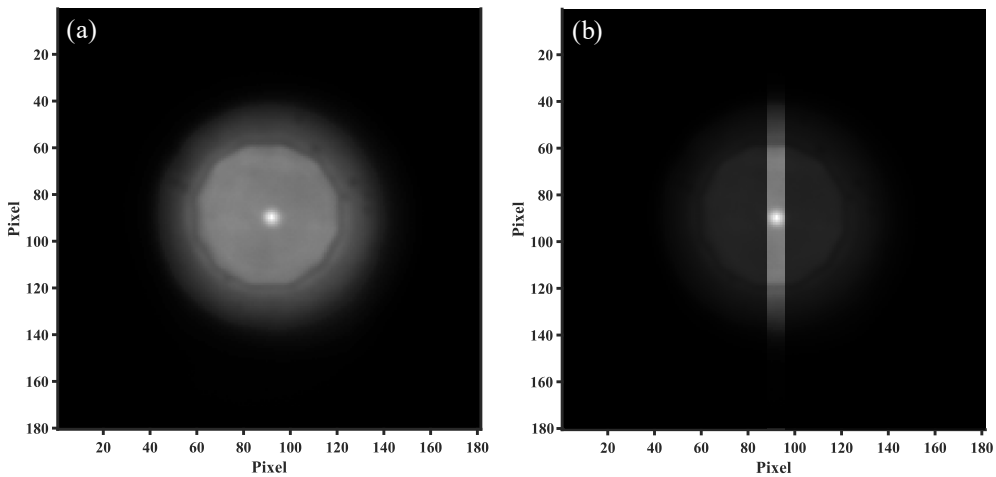

Figure 3.7: *(a) Visual depiction of an InP platelet illuminated with white light, with the excitation spot positioned at the center of the platelet. (b) The detection area from the platelet is minimized after closing the slit in front of the spectrometer. The slightly transparent black block in this illustration demonstrates how the slit covers the unwanted detection area.*

During SSPL, setting the spectrometer at 0^{th} order grating, the nanostructure image is captured by the CCD. Fig 3.7(a) shows the resulting image of a platelet illuminated with white light, with the laser excitation occurring in the middle of the

platelet. The white light serves the dual purpose of revealing the structure and ensuring that the laser excitation spot accurately hits the desired location. On the CCD, the x and y axes represent the spatial coordinates of the nanostructure. When focusing on spectral features, the vertical slit positioned at the image plane in front of the spectrometer is closed. This allows for the selection of a very specific detection area, as shown in Fig 3.7(b). Later the white light is turned off to exclusively capture information about the emission from the nanostructure. Subsequently, the spectrometer grating is set in the 1st order. The x-axis of the CCD records the dispersed wavelengths of the emission originating from the nanostructure. However, the y-axis still denotes the spatial coordinate of the nanostructure, as illustrated in Fig 3.8(b).

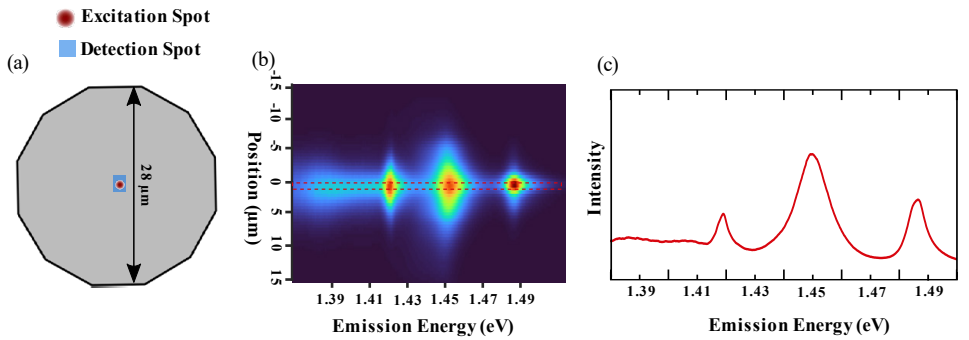

Figure 3.8: *(a) Diagram illustrating a platelet with identical size for the excitation and detection spots. (b) Emission from the platelet resolved both spectrally (x-axis) and spatially (y-axis). (c) Intensity profile of the selected area of the nanostructure (red dotted line in (b)) as a function of emission energy.*

Fig 3.8(b) illustrates the image projected on the CCD, where the x-axis represents the emission energy, and the y-axis is the spatial position along the arrows in Fig 3.8(a). As demonstrated in Fig 3.8(b), it is possible to integrate the spectral intensity along a horizontal cut. The section of horizontal cut reduces the detection area, as shown in Fig 3.8(a). From this horizontal cut, the spectral characteristics of the emission are identified, as depicted in Fig 3.8(c). By choosing an area away from the center, it is possible to study the emission away from the excitation spot.

In order to understand the spatial evolution of a specific emission, a vertical cut corresponding to that emission peak is selected, as depicted in Fig 3.9(b). The vertical cut enables the detection of emissions away from the excitation spot, capturing emissions from a larger detection area, as illustrated in Fig 3.9(a). The integrated spatial evolution of the selected spectra in Fig 3.9(b) is presented in Fig 3.9(c).

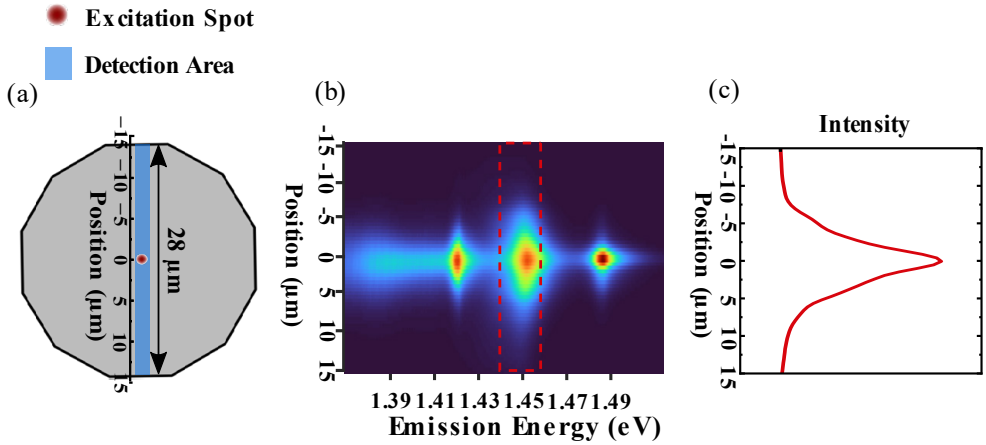

Figure 3.9: *(a) Illustration of a platelet featuring the excitation spot and the spatially resolved detection area. (b) Emission from the platelet resolved both spectrally (x-axis) and spatially (y-axis). (c) Intensity profiles of the chosen emission (red dotted line in (b)) are plotted against the position along the detection area outlined in (a).*

3.3.2 Time-resolved Photoluminescence Spectroscopy

In SSPL, information about emission spectra and spatial distribution of emission is obtained. TRPL primarily offers insights into the temporal evolution of emission spectra. As described above, the x-axis represents energy, and the y-axis the time evolution of the emission. In this case, a vertical slit is used at the entrance of the spectrometer. However, as an image of the sample is projected on the entrance plane of the spectrometer, it is possible to study the temporal expansion of the emission. Using a bandpass filter enables the extraction of spatial distribution over time for a selected emission energy. In this case, the vertical slit of the spectrometer is opened fully, and a horizontal slit is used to select an area on the sample.

It is previously discussed that the streak system records spectral information along the x-axis and temporal information along the y-axis. However, to select the detection area of interest, the emission is initially directed to a CCD camera before reaching the streak system. Once we define the detection area using a vertical slit in front of the spectrometer, we redirect the emission towards the streak system. In front of the streak system, a horizontal slit is employed to further narrow down the detection area, as depicted in Fig 3.10(a). The spectrometer grating is set in the 1st order. The x-axis of the CCD of the streak system records the dispersed wavelengths of the emission, and the y-axis records the temporal evolution of the emission, as shown in Fig 3.10(b). From this horizontal cut on the 3D image of Fig 3.10(b), the spectral characteristics of the emission are identified in Fig 3.10(c).

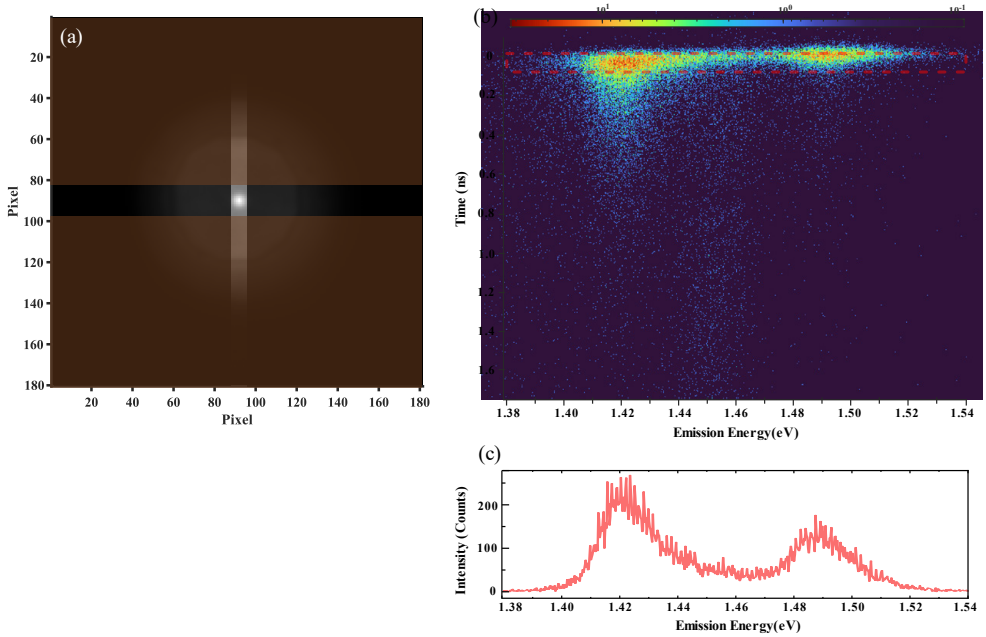

Figure 3.10: *(a) The detection area from the platelet is minimized after closing the slit in front of the spectrometer and streak system. The slightly transparent black block in this illustration demonstrates how the vertical slit covers the unwanted detection area. The transparent brown color block shows how the horizontal slit minimizes the detection area, covering a more defined region. (b) TRPL data x-axis denotes emission energy and the y-axis time after pulse excitation. In (c) the PL spectra (red curve) are extracted from the 3D image by the integration of spectral intervals (dashed red rectangle).*

To capture the temporal and spatial evolution of emission, the characterization of the emission spectra has to be sacrificed. A bandpass filter is employed in front of the spectrometer to select the specified emission energy of interest. Fig 3.10(b) illustrates the full spectral characteristics of the emission with time. By using a filter, it is possible to make a spectral selection, as shown in Fig 3.11(a) After selecting the specific emission energy, the spectrometer grating is changed from the 1st order to the 0th order, thereby sacrificing the spectral information. With the grating set at the 0th order, the spatial information of emission from the platelet in the x-direction is recorded, while the y-direction denotes the temporal evolution of emission. This makes it possible to study how the emission spreads after excitation. To capture spatial information from a larger area on the platelet, we open the slit widely in front of the spectrometer to detect emission from the entire platelet in the horizontal direction, as shown in Fig 3.11(b). This arrangement allows us to detect emissions away from the excitation spot. The spatial and temporal evolution of the selected emission spectra is presented in Fig 3.11(c), where the x-axis denotes the spatial coordinates, and the y-axis represents time.

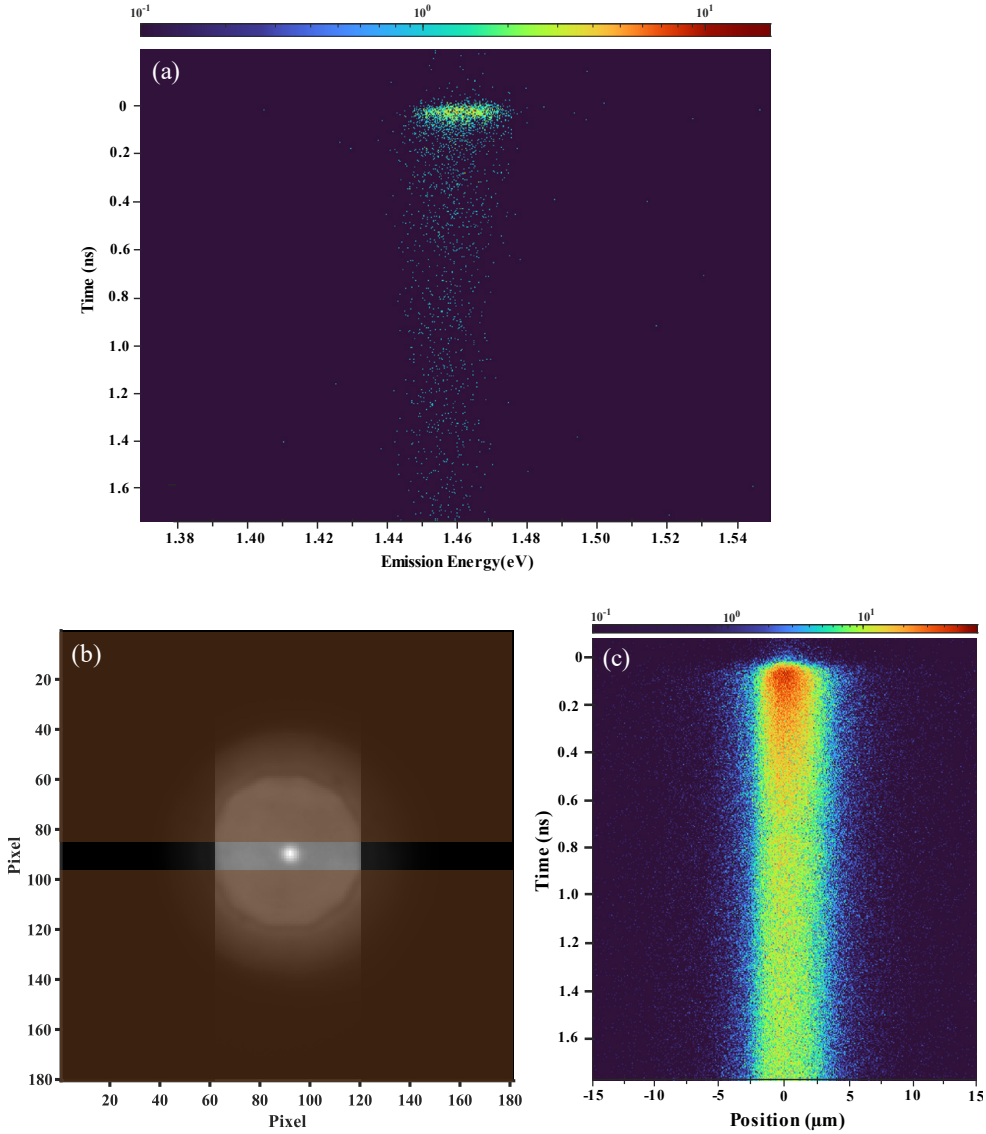

Figure 3.11: *(a) TRPL data displays the x-axis representing emission energy and the y-axis depicting time after pulse excitation, revealing a more focused emission spectrum. (b) By opening the slit in front of the spectrometer, the detection area from the platelet is maximized. (c) The presentation of spatial and temporal evolution in the selected emission spectra, with the x-axis representing spatial coordinates and the y-axis representing time.*

3.4 Scanning Electron Microscopy

Scanning Electron Microscopy (SEM) is a widely used characterization tool that offers enhanced resolution and the ability to examine small objects that are beyond which restricts the resolution to objects larger than 200 - 300 nm, an SEM employs electrons with significantly shorter wavelengths[63]. By utilizing electrons instead of visible light photons, the resolution can be improved to about 1 nm. Electron microscopes, as opposed to conventional optical microscopes, utilize electric and magnetic fields to control and focus the electron beam, as traditional lenses cannot be used for electron manipulation. An SEM system typically consists of an electron source, condenser lenses, scanning coils, an objective lens, detectors, and a specimen chamber. A high-vacuum environment is crucial from the electron source to the specimen chamber to minimize electron scattering caused by collisions with gas molecules. Magnetic condenser lenses control the trajectory and focus of the electron beam emitted from the electron source. The objective lens is responsible for precisely focusing the electron beam onto the sample surface, while the scanning coils enable meticulous two-dimensional raster scanning of the beam. The detecting electron count per raster point is then translated into an image.

In close proximity to the sample, one or more detectors can be placed to capture specific particles and signals generated by the interaction between the electron beam and the sample. The electron beam, accelerated by a voltage of the order of 10 kV, is focused and systematically scanned across the sample surface in a point-by-point fashion. At each point, the electron beam interacts with the sample, leading to the generation of primary electrons (such as backscattered electrons) and secondary electrons. Images using secondary electrons generally give an overall morphology of objects. The contrast is a mixture of topography, composition, and doping. Backscattered electrons on the other hand are sensitive to composition and topography, where the detector geometry can be selected to enhance either composition or topography. The resolution of an SEM typically ranges around 10 nm, although advancements have enabled achieving resolutions as fine as 1 nm.

3.5 Sample Preparation

Different approaches are employed to facilitate the optical characterization of the two distinct types of nanostructures (NWs and platelets) used in this thesis.

1. For NWs, conducting optical spectroscopy (PL) directly as grown on the substrate yields undesirable signals originating from the substrate itself, which is often composed of the same material as the NWs. Due to a much larger volume, the emission from the substrate is often much stronger than from the NWs itself. Consequently, the emission from the NWs can be drowned by the background emission of the substrate. It is also challenging to isolate the emissions from individual NWs since they are typically grown in close proximity on the substrate, and closely spaced, too closely to resolve individual NWs. To enable the study of individual NWs, they are mechanically broken off from the growth substrate and transferred onto a silicon substrate coated with a layer of gold. This gold-coated substrate is patterned with an indexed grid, allowing for the identification of individual NWs. Therefore, various optical spectroscopy techniques and SEM characterization can be performed on the same NWs. It is also possible to return to the same NW for additional measurements.

Figure 3.12: *A gold-covered Si substrate with a pattern enabling the identification of single NWs. Single NWs are indicated on the substrate by red rectangles.*

2. In the case of platelets, as the primary focus of interest lies in the interface between the substrate and the platelet, the substrate itself becomes an integral part of the nanostructure. The area of the individual platelets is generally significantly larger than the laser spot, making single platelet spectroscopy feasible. Furthermore, the significant spacing between platelets provides an opportunity to study them individually. Therefore, direct excitation of the platelets can be conducted, enabling their optical characterization. In addition, the platelets are grown in regular arrays and by counting lines and columns, it is possible to return to the same platelet using different techniques.

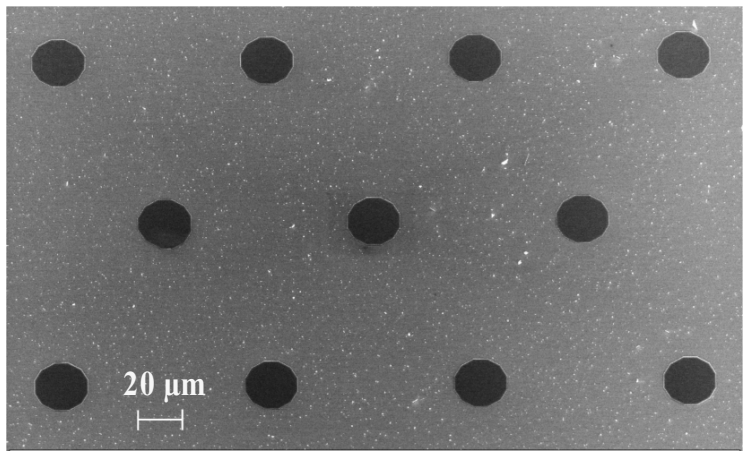

Figure 3.13. *SEM images of a specific section within the entire platelet array.*

4 Results

This chapter presents comprehensive investigations of the charge carrier dynamics at the type-II interface in wz/zb single interface heterostructured InP. The findings from three papers are summarized in this chapter: Paper-I focuses on the recombination dynamics of IXs at single wz/zb interface heterostructured InP NWs with a small interface area and a large influence of the radial surface. However, the small wz/zb interface cross-sections in NWs (<< 1 μm^2), pose challenges to investigations of the spatial distribution of IXs. In the case of platelets (interface area > 500 μm^2), having access to these larger interfaces significantly facilitates the examination of the spatial distribution of IXs along the type-II interface. Paper-II investigates the IX dynamics at the wz/zb single-interface of the heterostructured platelets. In Paper-III, insights are provided into the impact of doping on the transport of IXs for these platelets.

4.1 Heterostructured InP Nanowires

The first paper presents an investigation of power-dependent SSPL and TRPL of InP NWs[46]. These particular NWs contain one single wz/zb interface, which exhibits a type-II band alignment, as discussed in Chapter 2. Two types of NW samples are studied using optical measurements.

1. The first type consists of nominally undoped wz/zb NWs, grown from nominally 30 nm diameter gold (Au) seed particles[64]. The individual wz/zb NWs have an average wz length of 2 μm and a single zb top segment of approximately 200 nm in length.
2. The second sample type consists of n-type doped NWs, with similar geometry as the undoped NWs, where the wz -InP core is doped with sulfur, making it degenerately n-type, while the zb top segment remains nominally undoped.

The study mainly explores the recombination properties of IXs at the type-II interface and investigates the influence of doping on the IXs emission, comparing both types of NW architectures.

4.1.1 Undoped wz/zb InP nanowires

In our study, we first provided evidence of the presence of a type-II interface in our sample by observing two important features. First, the IX emission is expected to exhibit a red-shifting peak with reduced EPD of the continuous excitation, as discussed in section 2.3. We have conducted power-dependent SSPL on type-II InP NWs to confirm this behavior.

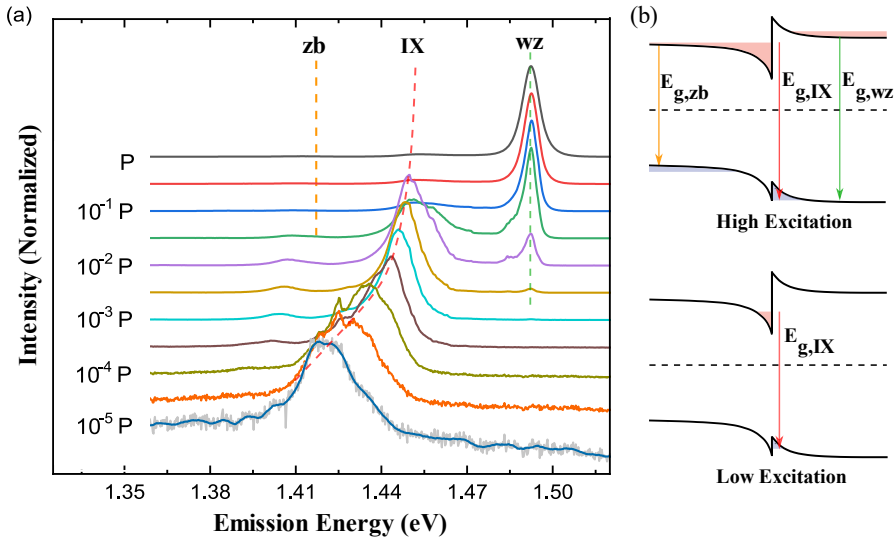

Figure 4.1: *(a) Normalized power-dependent PL spectra of an undoped single wz/zb InP NW as a function of EPD. (b) Band diagram of the type-II interface: Schematic explanation of the red shift of emission with reducing EPD from high (upper panel) to low (lower panel).*

The results of the undoped wz/zb NWs are discussed first. Fig 4.1(a) presents the normalized power-dependent PL spectra of a single undoped type-II InP NW. Each spectrum is normalized to its maximum value (irrespective of the most intense peak) and they are displaced relative to each other for clarity and comparison purposes. The emission peaks at 1.49 eV and 1.42 eV correspond to the bandgap emissions of wz InP and zb InP, respectively. The emission peak in the spectral range of 1.45 eV to 1.42 eV that shifts with EPD is attributed to the IX emission. The peak position of the IX emission undergoes a redshift of 30 meV as the EPD (P) decreases by five orders of magnitude. The redshift occurs because, at low EPD, the potential wells on both sides of the interface are less filled, as compared with the higher filling of the potential well at high EPD. At lower EPD, it is possible to observe the IX emission peak below the bandgap of zb InP (not shown). The details regarding charge carrier confinement and the dependence of the IX emission on the EPD are discussed more comprehensively in section 2.3.

Second, the IX emission is expected to exhibit a long recombination time after an excitation pulse due to the spatially separated electron and hole wavefunctions at the type-II interface. To investigate the dynamics of the IX emission, TRPL measurements were utilized.

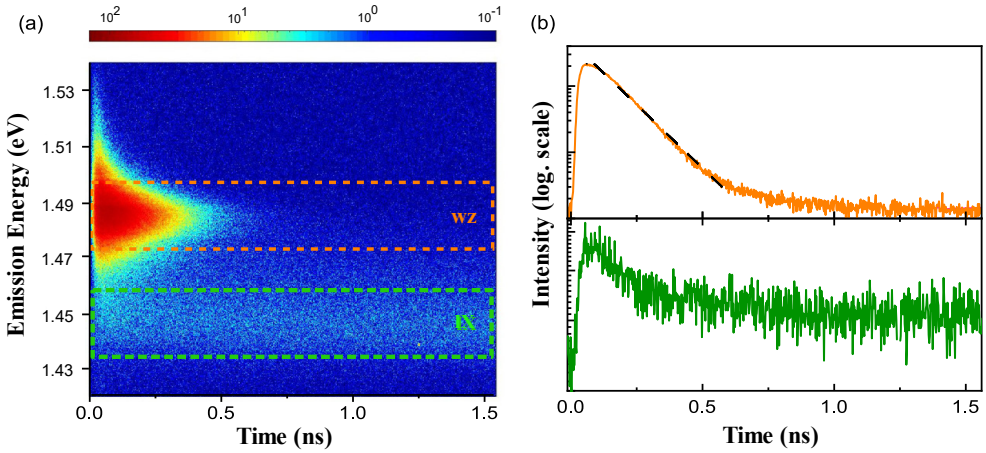

***Figure 4.2**: Time-resolved photoluminescence of a single, heterostructured NW with a single type-II interface. The false-color plot represents the time evolution of the PL after excitation by a laser pulse at time 0. The time evolution of the PL peaks corresponds to the cuts in the plot, indicated by dashed lines and shown in the graph on the right side with the corresponding colors. The black dashed line represents a linear fit to the experimental data of the wz emission in log scale indicating a single exponential decay.*

The obtained TRPL data (Fig 4.2(b)) revealed the decay profile of the photogenerated charge carriers. The band-to-band transitions of wz and zb InP could be described by a single exponential decay. When plotting the decay profiles on a semi-logarithmic scale (logarithmic intensity vs. linear time), a straight line was observed, indicating a constant recombination rate. The constant recombination rate is a consequence of the time-independent overlap of the wavefunctions following the pulsed optical excitation, as detailed in section 2.3. Due to the complete overlap of the wavefunctions, the wz emission exhibited a faster recombination rate, resulting in a relatively short emission lifetime of 260 ps. In contrast, the decay profile of the IX emission exhibited a non-exponential characteristic, indicating a time-dependent recombination rate. Consequently, fitting the decay profile with a single exponential decay was not feasible. The temporal behavior of the recombination rate of IXs, in relation to the penetration of wavefunctions through the barriers, is discussed in section 2.3. In this context, the slope of the decay gradually diminishes, signifying a decrease in the recombination rate with time. This is in accordance with a reduced wavefunction overlap. Notably, a significant IX emission persists even 30 ns after the excitation, as illustrated in Fig 4.3. This is

especially noticeable at the highest EPD (P). This long-lived emission is attributed to the slow recombination rate resulting from the limited overlap of the electron-hole wavefunctions of IXs.

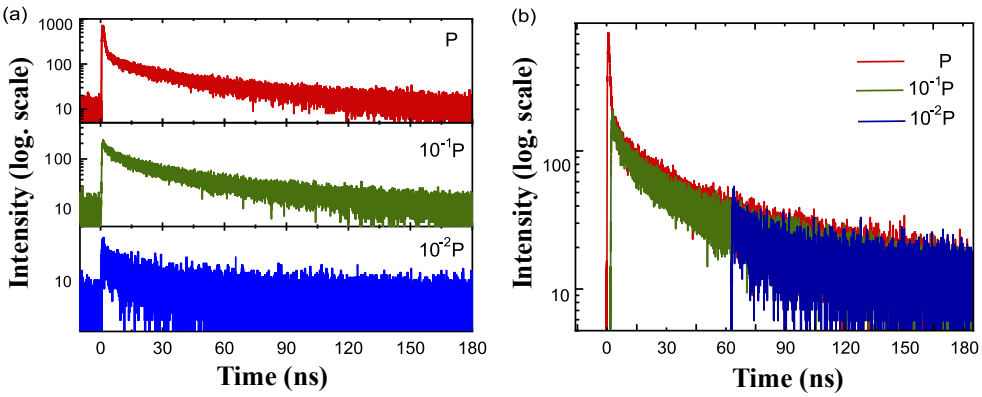

Figure 4.3: *(a) Power-dependent PL decay shows a non-exponential behavior (recorded at different excitation power densities of an undoped single interface wz/zb NW). (b) The traces in (a) have been shifted in time such that the initial emission intensity is the same. The time evolution is then seen to be the same.*

To support the explanation of a time-dependent recombination rate as a function of charge carrier density in the potential wells, a series of time traces were recorded using different EPDs, as shown in Fig 4.3(a). As discussed in section 2.3, the higher up the charge carriers are positioned in the well, the larger the part of the wavefunction that extends across the interface. When a higher EPD (P) is applied, the potential wells are initially filled up higher within the potential well. This results in larger wavefunction overlaps and thus a faster recombination rate in the early time window after the excitation pulse. In contrast, for lower EPD (e.g., 10^{-2} P), the initial recombination rate is slower due to the limited overlap of the wavefunctions as a result of the initial occupation of the less filled potential well. Comparing the decay profiles at different EPDs allows us to observe the temporal evolution of the IX emission starting at different times. With a high EPD, the potential wells on both sides of the interface are initially filled to a higher level with a certain charge carrier density. As time elapses after the excitation pulse, the density of the IXs gradually decreases due to recombination, leading to a depletion of IXs in the potential well. Eventually, at a specific point in time, the IXs density reaches the same level as that achieved after an excitation pulse with a lower EPD. From that moment onward, the decay profile obtained after the high EPD pulse aligns with the decay profile recorded with a lower EPD. This can be visualized by shifting the decay profile of the lower EPD by a specific time interval to achieve an overlap of the profiles. In Fig 4.3(b), it is evident that the decay profile for the EPD of P closely follows the

trace of 10^{-1} P after 2 ns and the trace of 10^{-2} P after 60 ns, respectively. This observation shows that the time evolution is Markovian[65]. In a Markovian system, the probability of transitioning to any particular state depends solely on the current state, not on how the system arrived at its current state. In simpler terms, a Markovian process has no memory of its past states beyond its current state. The future behavior of the system is determined only by its present state. Here also only the charge carrier density at the time affects the subsequent time evolution.

4.1.2 n-type doped wz/zb InP nanowires

In addition to looking into the behavior of undoped NWs, we have also investigated the case of n-type doped ones to explore the influence of a two-dimensional electron gas (2DEG) on the recombination dynamics. In our study, the wz segment of the NW was intentionally subjected to high doping levels. The consequence of the doping is that the potential well for electrons is fully occupied, even in the absence of external excitation. This unique characteristic of the highly doped wz segment establishes a significant presence of electrons within the system, contributing to the formation of a 2DEG at the interface.

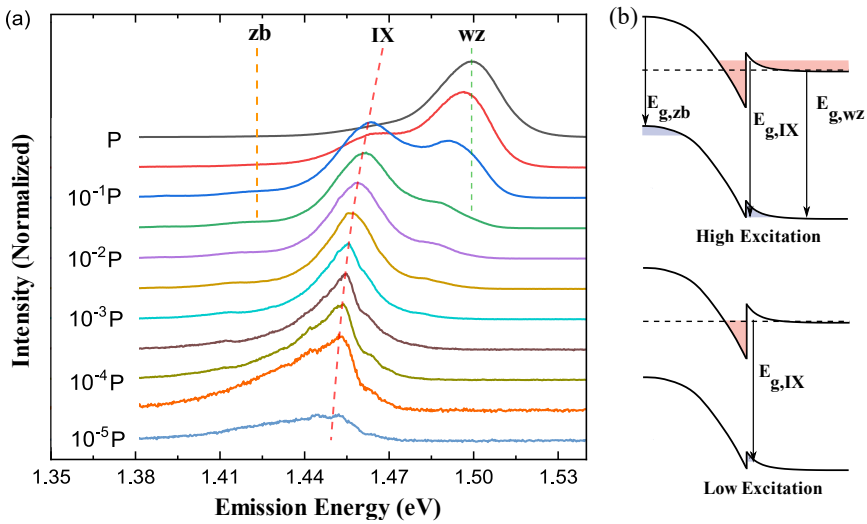

Figure 4.4: *(a) Normalized, power-dependent PL spectra of an n-type doped single wz/zb InP NW as a function of EPD. (b) Band diagram of the type-II interface: Schematic explanation of the red shift of the IX emission when reducing the EPD from high (upper panel) to low (lower panel).*

In the case of n-type doped wz/zb NWs, we have observed distinct differences in the dependence of emission energy on the EPD and recombination rate compared to undoped NWs. Fig 4.4 illustrates a series of power-dependent SSPL spectra of an

n-type doped type-II InP NW. Similar to the presentation in Fig 3.1 for the undoped case, the spectra are also normalized and displaced in the doped case. Again, we detect the IX emission, and it undergoes a redshift as the EPD decreases. However, the shift is only 10 meV, which is considerably smaller than the 30 meV shift observed in undoped InP NWs, despite both types of NWs experiencing the same order of magnitude in variations of the EPD densities. In the case of the n-type doped NWs, the electron density within the potential well remains essentially independent of the EPD due to the substantial number of electrons introduced by the n-type doping. As the EPD varies, the relatively minor redshift observed in the IX emission can be attributed mainly to variations in the filling of the potential well for holes. Moreover, the wz band gap emission peak of the doped NWs displays a broader profile, which can be attributed to the high doping concentration present in the system [66].

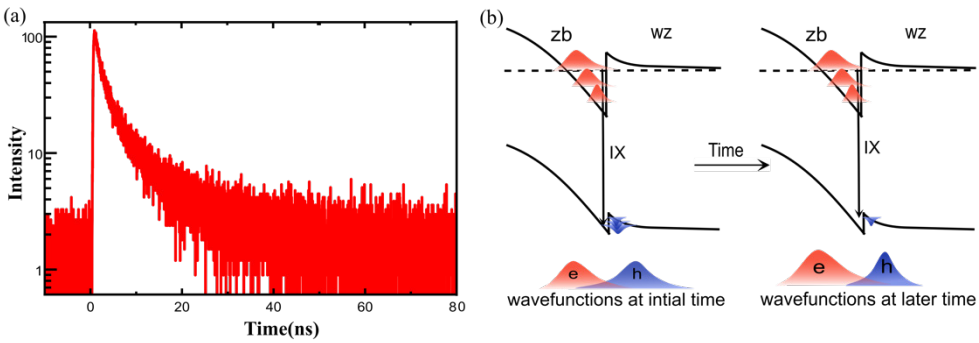

Figure 4.5: *Time-dependent decay of PL intensity of the IX emission of an n-type doped wz/zb NW. (a) shows the PL intensity decay profile on a log scale. (b) A schematic explanation for the temporal evolution of the overlap of wavefunctions for holes and electrons at the interface: At early times, high energy holes have a large overlap of their wavefunction with the electron wavefunctions. The overlap becomes smaller at later times since the filling in the potential well for holes decreases. The wavefunctions were normalized by scaling them to the peak of their respective wavefunctions. This normalization process was performed to facilitate a comparative analysis of the wavefunctions, allowing for improved clarity and visibility in their representation. The x-axis of the wavefunctions is expanded compared with the band diagram.*

Having first focused on the steady-state response of the IX emission in n-type doped NWs, we now focus on the recombination dynamics. In Fig 4.5, the decay profile illustrates a faster recombination rate for the doped case, attributable to the presence of numerous electrons per hole, which enhances the recombination rate. Consequently, the intensity of the IX emission from doped NWs diminishes significantly within 10 ns, contrasting with the 30 ns observed in the undoped scenario. The faster recombination rate contributes to an overall increase in the intensity of emissions from doped NWs compared to undoped NWs. The recombination rate in doped NWs also displays relatively less variation with time

compared with the decay profile of undoped NWs. After the excitation pulse, the penetration of the hole wavefunctions changes with time, while for the electron wavefunction the penetration through the barrier remains relatively constant. As a result, the temporal change in the overlap of wavefunctions is lower compared with the case of undoped NWs, resulting in a lower impact on the recombination rate with time after the pulse.

4.2 Heterostructured InP Platelets

The second and third papers are dedicated to studying the spatial and temporal dynamics of IXs at the type-II interface, particularly in large-area InP wz layers (> 500 μm^2) that are grown on top of zb InP substrates[47]. In this case, the majority of the type-II interface is located far away from the side walls of the platelet, where the influence of potential non-radiative recombination on the side wall is significantly reduced, as compared with the NW case. The availability of these large-area interfaces provides a unique opportunity to investigate the spatial distribution of excitons with greater ease and larger distances, several μm. Moreover, in the case of platelets, there is a considerable reduction in the influence of surface effects compared to NWs.

To observe the variations in the spatial and temporal dynamics of IXs in the presence of an electron gas, we conducted a comparative analysis between two types of platelet samples: one with a nominally undoped wz/zb type-II interface and the other with an n-type doped wz/zb type-II interface. In the latter type, the wz segment of the platelet is doped with sulfur (S), resulting in n-type characteristics, while the zb substrate remains nominally undoped.

We utilized spatially resolved SSPL and TRPL to investigate both the spatial distribution and recombination dynamics of IXs along the type-II interface. For optical investigation, two types of methodologies were employed based on the detection of emission:

1. Non-Spatial Detection: To provide evidence of the presence of a type-II interface in our sample, similar to the wz/zb NWs, not spatially resolved SSPL and TRPL were initially performed where emissions are collected from smaller areas close to the laser spot.
2. Spatial Detection: Subsequently, after confirmation, we performed spatially resolved detection using both SSPL and TRPL techniques to gain insights into the spatial profile of IX emission. Both methods are discussed in detail in Chapter 3.

4.2.1 Steady-state Photoluminescence

To obtain the first evidence of the presence of a type-II interface in our sample, we conducted power-dependent SSPL measurements on our wz/zb InP platelets, maintaining the excitation and detection spots at the same positions. The emission from the IXs is expected to show a red-shifting peak with decreasing EPD under continuous excitation, indicative of reduced filling of the potential wells. This phenomenon is discussed in the context of NWs in the previous section.

The obtained spectra were normalized and analyzed for varying EPD, as shown in Fig 4.6(a) and Fig 4.6(c) for undoped and n-type doped platelets, respectively. The spectral lines at 1.49 eV (labeled wz) and 1.41 eV (labeled zb) were attributed to charge carrier (or direct exciton) recombination in the bulk wz platelet and zb substrate, respectively. For undoped platelets, our results revealed the IX emission peak in the spectral range of 1.45 to 1.41 eV in Fig 4.6(a), exhibiting a redshift of approximately 40 meV as the EPD decreased. This behavior of the IX peak agrees with the observations in NWs from the previous section, supporting the presence of a single type-II interface in the InP platelets.

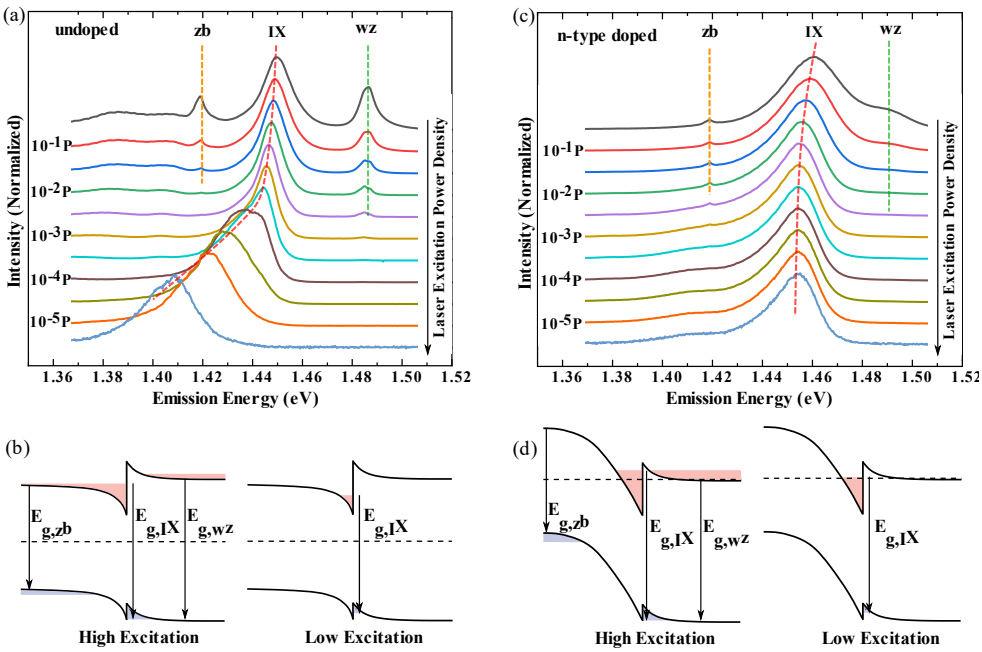

Figure 4.6: *Normalized, power-dependent PL spectra of (a) an undoped InP platelet and (c) an n-type doped InP platelet as a function of EPD. Band diagram of the type-II interface of (b) an undoped platelet and (d) an n-type doped InP platelet. Schematic explanation of the red shift of emission with reduced EPD from high (left panel) to low (right panel). In the doped case, the redshift is significantly less as compared with the undoped case.*

However, the IX emission for the n-doped platelets experiences a redshift of only 5 meV (from 1.455 to 1.460 eV) as the EPD decreases in Fig 4.6(c). This shift is notably smaller than the shift observed in undoped InP platelets in Fig 4.6(a), despite a similar change in EPD. Fig 4.6(b) and Fig 4.6(d) schematically illustrate the occupation of IXs in the triangular potential well under high and low EPD conditions for an undoped platelet and an n-type doped platelet, respectively. The difference in shift for the n-doped sample compared to the undoped platelet is similar to the features of nominally undoped and doped NWs discussed earlier. The relatively minor shift in the IX emission for the n-type doped platelet primarily arises from variations in only the filling of the potential well for holes as the EPD varies, providing evidence for the presence of the electron gas due to doping for this type of platelet sample architecture as well.

4.2.2 Time-resolved Photoluminescence

To obtain the second piece of evidence indicating a longer recombination time for IX, we conducted TRPL while keeping the excitation and detection spots fixed at the same positions.

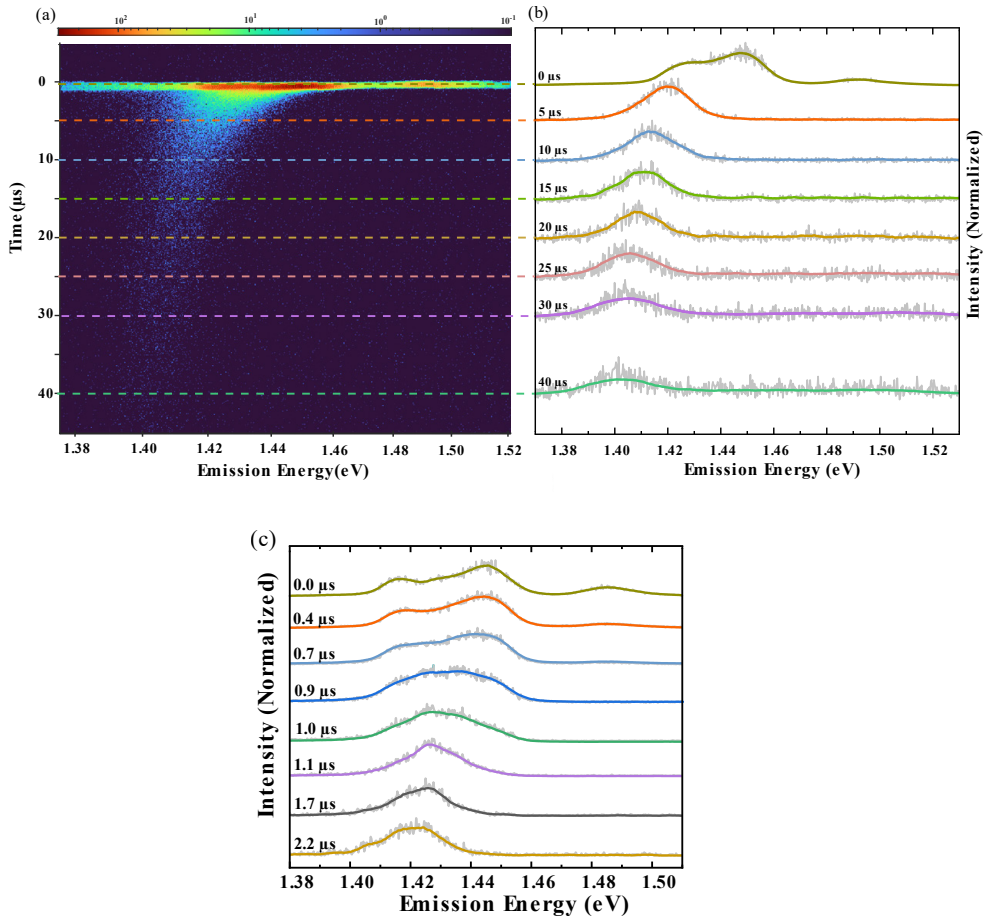

Figure 4.7: *(a) TRPL of a platelet with a type-II heterojunction. The false-color plot represents the spectrally resolved temporal evolution of the PL after excitation by a laser pulse at time 0. (b) The PL intensity integrated over time windows of 3 μs at different delays after the pulse. The normalized evolution of the emission spectra corresponds to the horizontal cuts in the false-color plot, indicated by dashed horizontal lines and shown in the graph with the corresponding colors. (c) The PL intensity integrated over time windows of 0.3 μs at different delays after the excitation pulse.*

The IX emission is expected to exhibit a long recombination time after the excitation pulse due to the spatially separated electron and hole wavefunctions at the type-II interface. The streak scope image in Fig 4.7(a) illustrates the temporal evolution (y-

axis) of the PL emission intensity as a function of the energy of the emitted photons (x-axis). Notably, in Fig 4.7(a), the PL emission from the IX recombination in the platelet remains observable even 40 µs after the excitation, whereas in the NWs (as shown in Fig 4.3), the IX emission becomes negligible within a significantly shorter duration of 200 ns. This variation can be ascribed to the surface area of the NWs, where the entire type-II interface is in close proximity to the side walls, within the diffusion distance. Consequently, the side walls provide an alternative, non-radiative recombination route for the IXs, impacting the recombination dynamics of the IX emission. In contrast, the platelet structure, with the majority of the interface being distant from the side walls, faces relatively minimal competition from this alternative non-radiative recombination pathway. This allows for extended observation time of PL emission resulting from the IX recombination.

As previously discussed regarding the redshift of the IX emission in power-dependent SSPL measurements and shown in Fig 4.6(a) for platelet samples, we also observe a redshift in the IX emission in TRPL data. The redshift amounts to approximately 50 meV with increasing time after the excitation, as evident in the extracted time traces presented in Fig 4.7(b). The PL spectra displayed in Fig 4.7(b) are derived from horizontal cuts of the 3-dimensional dataset in Fig 4.7(a), and the evolution of the PL spectra with time after excitation (integrated over a time interval of 3 µs) is illustrated in Fig 4.7(b). This time-dependent peak shift, a behavior akin to the one observed in the power-dependent SSPL, hints at the similar mechanism discussed before, a depletion of the potential wells at the interface.

We now take a closer look at the recombination dynamics. At the initial time after the excitation pulse (t = 0 µs, integrated over the 3 µs time range), the potential wells on both sides of the interface are filled with charge carriers, resulting in recombination from the higher energy levels and therefore higher emission energy, as shown in Fig 4.7(b). The likelihood of recombination at higher energies was discussed in the NW section in terms of increased spread of the wavefunctions and therefore more penetration through the barriers, leading to a larger overlap of the wavefunctions. However, as time elapses after the excitation pulse, the potential wells start to deplete, leading to a redshift of the IX emission peak down to 1.40 eV after 40 µs. The shift of peak is very abrupt at t = 0 µs and 5 µs in Fig 4.7(b). To interpret the peak shift during the initial period from 0 µs to 2.5 µs, we take a closer look with a finer integrated time range of 0.3 µs as illustrated in Fig 4.7.(c).

The previously utilized longer time scale window (50 µs) was not well-suited for a comprehensive capture of the depletion of the potential well due to the lower temporal resolution. To obtain more details about the change in the overlap of wavefunctions with different occupations of the energy levels of the potential well, the recombination dynamics of the IXs were measured on a shorter time scale (1 µs), as illustrated in Fig 4.8(c).

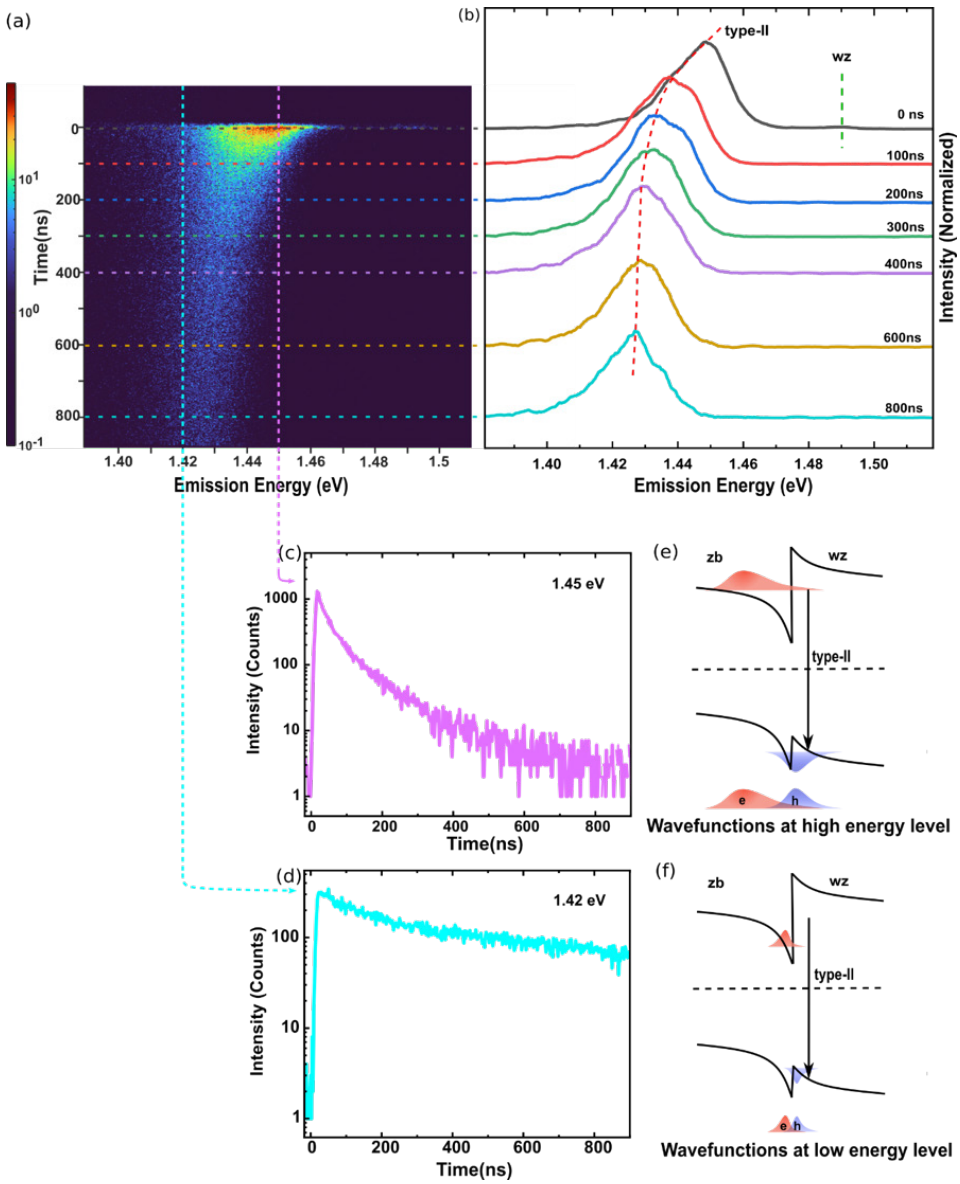

Figure 4.8: (a) TRPL of a platelet with a type-II heterojunction. The false-color plot represents the spectrally resolved time evolution of the PL after excitation by a laser pulse at time 0 ns. *The EPD is low in order to show a spectrum that is dominated by the IX emission.* (b) The PL intensity is integrated over time windows of 10 ns at different delays. The normalized evolution of the emission spectra corresponds to the horizontal cuts in the false-color plot, indicated by dashed horizontal lines and shown in the graph with the corresponding colors. (c-d) The time evolution of the PL peaks corresponds to the vertical cuts in the false-color plot, indicated by dashed vertical line lines. The intensity is integrated over energy windows of 10 meV. (e-f) Schematic explanation of the overlap of the wavefunctions for holes (h) and electrons (e) at the interface. For the high energy levels of the IX emission, the overlap is larger, whereas, for the low energy level of the IX emission, the wavefunctions have a smaller overlap.(Taken from SI-Paper-II)

In the discussion of NWs earlier, a faster recombination rate is expected at higher energy levels due to the larger wavefunction overlap. Conversely, a smaller overlap of the wavefunctions at lower energy levels results in a slower recombination rate. This expectation is supported by Fig 4.8(c), where the higher energy level emission at 1.45 eV exhibits a faster or sharp decay profile. Meanwhile, Fig 4.8(d) corresponds to the lower energy level with an emission at 1.42 eV, showing a slower decay profile.

After discussing the recombination dynamics of IXs in the undoped platelet, we investigate the effect of doping on recombination dynamics. Fig 4.9(a) illustrates the temporal evolution of the IX emission intensity for the n-type doped platelet. In Fig 4.9(b), the decay profiles of IX emission for the doped and undoped platelets are presented, revealing a faster recombination rate with a sharp decay for the doped platelet whereas the IXs are long-lived in the undoped platelet. As discussed above, the presence of numerous electrons per hole enhances the recombination rate in the doped platelet.

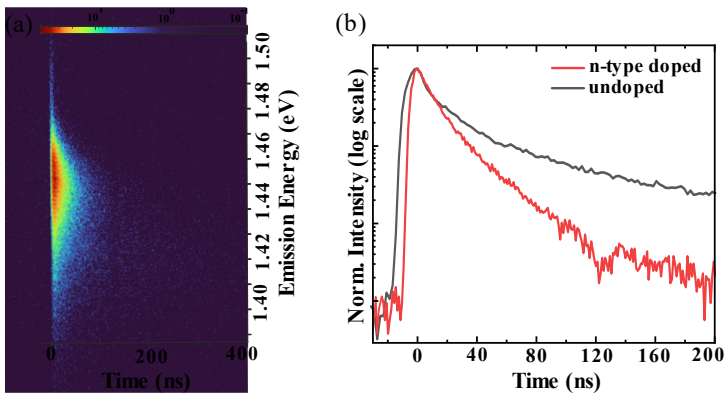

Figure 4.9: *(a) Time-resolved photoluminescence analysis of an n-type doped platelet. The false-color representation depicts the temporal evolution of the PL spectrum after pulse excitation by at t = 0. The EPD is low to show a spectrum that is dominated by the IX emission. (b) Time-dependent decay profiles of the PL intensity for IX emissions from both doped and undoped samples. The time traces have been aligned to the maximum intensity for t = 0 ns.*

To facilitate the comparison of rise times, we defined the time of the maximum intensity as t = 0 ns and aligned the profiles for the two platelet types. A prolonged rise time was observed in the undoped samples in contrast to the doped samples. In undoped samples, the necessity to capture both electrons and holes into the potential wells contributes to the prolonged rise time, while in the doped case, only holes need to be captured, given the pre-existing electrons due to doping. The rise time is dictated by the slowest capture rate, and it is evident that electrons are captured at a slower rate in undoped samples compared to holes in doped samples.

4.2.3 Spatially Resolved Steady-State Photoluminescence

Having established the presence of IXs in our sample, our attention turns to investigating their spatial distribution. To delve into the specifics of IX characteristics, we conducted measurements to observe how the IXs distribute spatially during the recombination process. A CW laser was accurately focused onto the central region of the platelet, resulting in the generation of excitons that move in all directions. Further details on the spatially resolved SSPL technique are provided in Chapter 3.

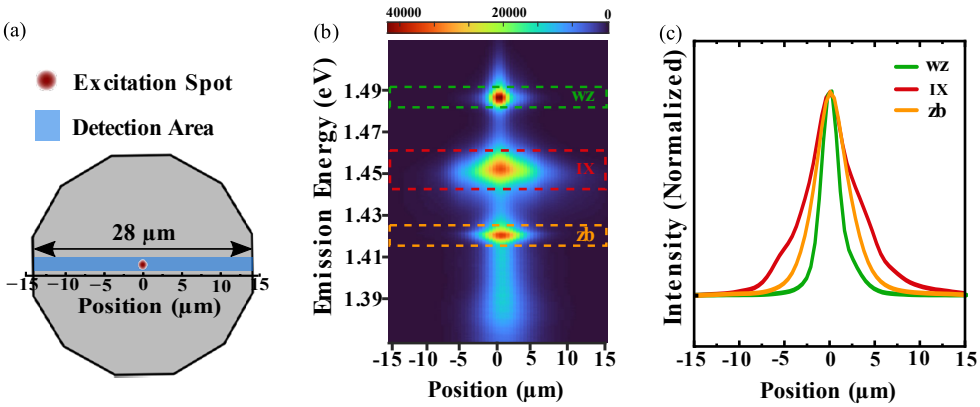

Figure 4.10: *(a) Schematic of a platelet with the excitation spot and the spatially resolved collection area. (b) Spectrally (x-axis) and spatially (y-axis) resolved emission from the platelet. (c) Intensity profiles of the zb, type-II, and zb emission as a function of position along the detection area in (a).*

The spatially and spectrally resolved SSPL image is depicted in Fig 4.10(b). For clarification, the integrated intensity for the spatial profile of the selected energies is plotted in Fig 4.10(c), corresponding to the marked areas (dotted lines) in Fig 4.10(b). This plot reveals that the spatial extent of wz and zb emissions is less pronounced than that of IXs. The full width at half maximum (FWHM) of the laser spot was determined to be less than 1 µm. The FWHM of the spatial extent of the bandgap emission from wz and zb was observed to be small, measuring only 3 µm. This limited spread is attributed to a fast recombination rate of direct excitons in wz and zb, which prevents them from spreading out significantly before recombination. On the contrary, at the type-II interface, the IXs exhibit a greater distance of travel away from the excitation spot before undergoing recombination. This extended travel distance is attributed to the substantially slower recombination rate of IXs, rendering them considerably long-lived.

To investigate the influence of EPD on the spatial profile, we plotted the spatial profile of emission for different EPDs in Fig 4.11. The EPD-dependent spatial

profile of the IX emission is shown in Fig 4.11(a), revealing a notable increase in spatial spread at higher EPD. This observation indicates a shift in the transport dynamics of the IXs from diffusive to repulsive force-driven mechanisms at high EPD. The distinct mechanisms of diffusive and repulsive force-driven transport are discussed in detail in section 2.4. This behavior contrasts with the diffusive spatial spread of emission from other segments, such as wz and zb, which remains unchanged even at high EPD, as shown in Figs 4.11(b) and 4.11(c), respectively.

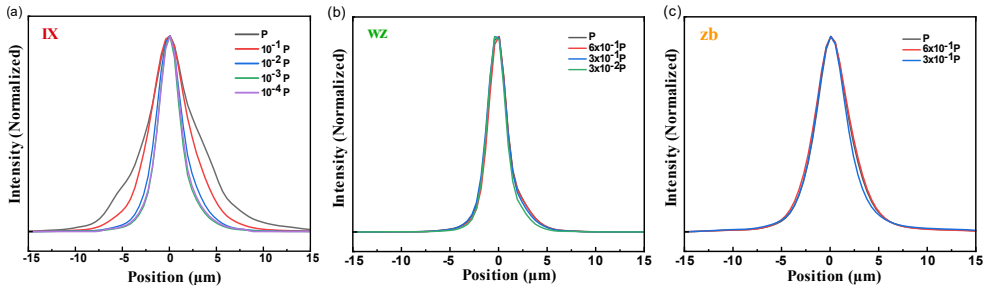

Figure 4.11: *Spatial profiles of emission as a function of position (distance from the excitation spot center) for various EPDs. (a) Demonstrates the EPD-dependent spatial profile of IX emission, while (b) and (c) illustrate the consistent spatial extent of wz and zb emissions, respectively, across different EPD conditions.*

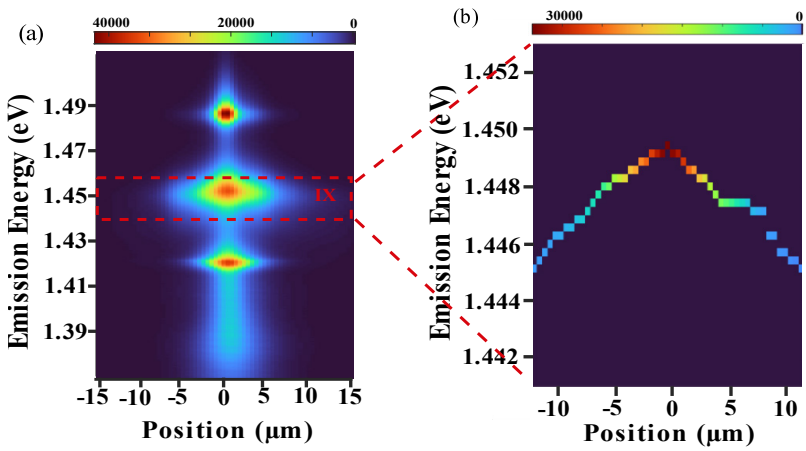

Figure 4.12: *(a) Spectrally and spatially resolved emission from the platelet. (b) The peak of the IX emission as a function of position, where the color map denotes the intensity.*

Moreover, there is a correlation between the emission energy of the IXs and their distance from the excitation spot, as illustrated in Fig 4.12(b). The energy of the IX recombination is influenced by the local IX concentration. In the excitation spot, the

concentration is the highest, resulting in a high degree of filling in the potential wells and, consequently, the highest energy of the IX recombination, as previously discussed for varying EPD. As the IXs move away from the excitation spot, their density decreases, leading to a reduced filling of the energy levels within the potential wells. This reduction results in the IX emission peak energy shifting towards lower values for locations away from the excitation spot. This observation agrees with the redshift of the IX emission observed in power dependent SSPL, as shown in Fig 4.6(a).

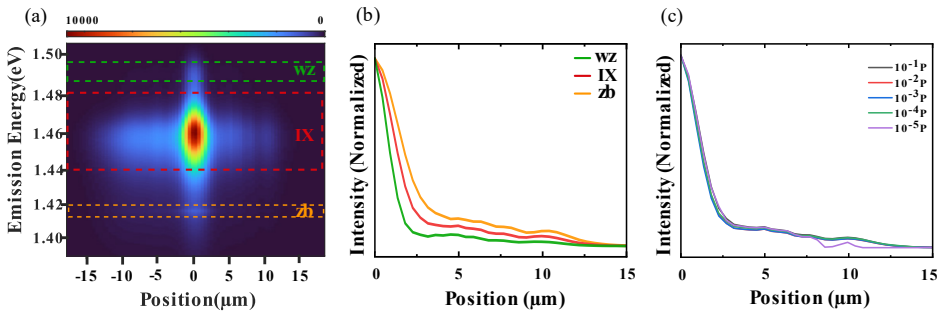

Figure 4.13.: *(a) Presentation of spatially (x-axis) and spectrally (y-axis) resolved emission from the doped platelet, represented in false color. (b) Depiction of the spatial distribution of the intensity of the emission spectra corresponding to half of the horizontal cuts in the false-color plot, indicated by dashed horizontal lines and illustrated in the graph with matching colors. The spectra were normalized to the highest intensity. In (c), intensity profiles of the IX emission are shown as a function of position (distance from the excitation spot) for different EPDs. The spectra are normalized to the highest intensity.*

Following an in-depth examination of the spatial distribution of IXs within the undoped platelet, our focus now shifts towards exploring the influence of doping on spatial dynamics. To explore the doping effects, Fig 4.13(a) presents spectrally resolved spatial profiles of the emissions from the doped platelet. The emission lines corresponding to wz, IX, and zb, extracted from spectral maps like Fig 4.13(a), are illustrated in Fig 4.13(b). Noteworthy differences in the spatial distribution of excitons between doped and undoped platelets are observed.

Firstly, the spatial profile of the IX emission in the doped sample is narrower than in the undoped platelet. The faster recombination rate due to doping constrains the spatial distribution of the IXs from the excitation spot in the doped platelet. It also exhibits a narrower spatial distribution of the IX emission compared to the zb emission, attributed to the background of electrons in the zb potential well impeding IX transport.

Secondly, the spatial distribution of the IXs shown in Fig 14.13(c) for the doped sample is independent of EPD, unlike the behavior observed for the undoped platelet

in Fig 4.11(c). In undoped platelets, repulsive interactions dominate at high EPD, facilitating longer-distance transport. Conversely, at low EPD, the IXs travel shorter distances primarily due to diffusion. In doped platelets, the presence of a large number of electrons from doping screens the repulsive interactions between aligned IX dipoles even at high IX density. We anticipate diffusive IX transport at higher EPD in n-type doped samples compared to the undoped samples. Achieving a high IX density is challenging in n-type doped samples due to the significantly faster recombination rate.

Thirdly, a discernible reduction in the spatial distribution of excitons is noted in the doped wz segment compared to the undoped platelet. The spatial profile of wz emission closely matches the laser excitation spot profile, with FWHM of approximately 2 μm. The presence of dopants causes the excitons to travel shorter distances from the excitation point in the doped wz segment. However, the spatial distribution of the zb emission remains essentially unchanged between doped and undoped platelets, consistent with expectations based on having used identical substrates.

4.2.4 Spatially Resolved Time-resolved Photoluminescence

After exploring the spatial distribution of IXs, our focus shifts to investigating the temporal evolution of the spatial distribution. Due to the fast spatial transport of the IXs, we narrowed our observation window to a very small time frame (2 ns) to observe the temporal impact of spatial distribution.

Figs 4.14(a) and 4.14(c) show spectrally resolved emission after pulsed excitation from undoped and doped platelets, respectively. The data is presented in a 3D image, with emission energy (eV) along the x-axis, time (ns) along the y-axis, and emission intensity color-coded. To discern the spatial profile, a filter is applied to capture emission within a specific IX energy range (1.450-1.467 eV), allowing us to trace the continuous expansion of the IX emission outward from the excitation laser spot in a spatially resolved manner. Further insights into the spatially resolved TRPL measurements are detailed in Chapter 3. However, it is noteworthy that the filter cannot exclude contributions from both wz and zb emissions initially, within the first 200 ns of the laser pulse. The PL spectra at t = 0 for undoped and doped platelets, reflecting the initial exciton density, are presented in Fig 4.14(b) and Fig 4.14(d), respectively. During the initial post-pulse excitation period, the spatial profile encompasses contributions from both wz and zb emissions, making the separation from the IX emission challenging before 200 ps. Consequently, data before 200 ps is excluded in the analysis of Fig 4.15.

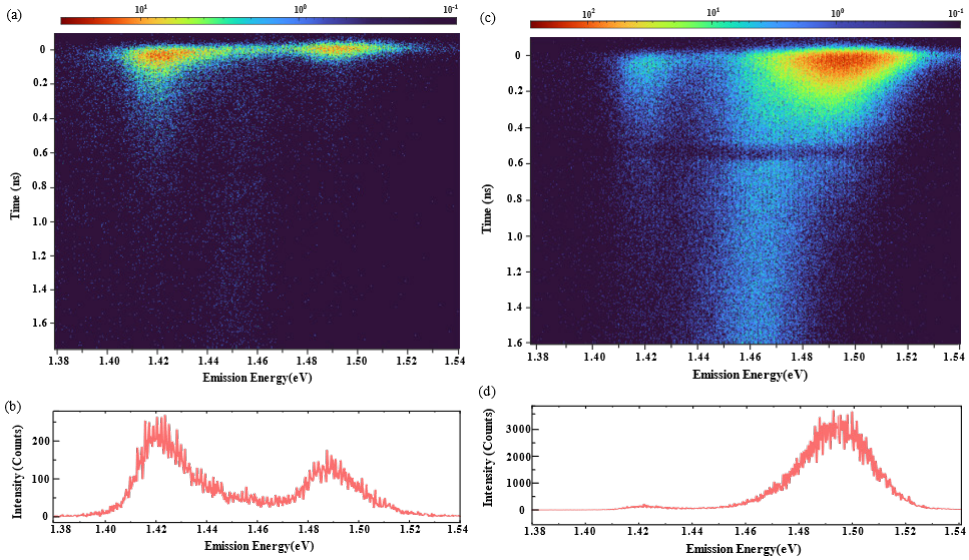

Figure 4.14: *TRPL analysis of (a) undoped and (c) doped platelets. The false-color representation depicts the temporally evolving PL spectrum after excitation by a laser pulse at time 0. The extracted spectra at t = 0 are shown for (b) undoped and (d) doped platelets: PL intensity integrated over time windows of 200 ps. After 200 ps the the influence of the wz and zb emission became insiginificant.*

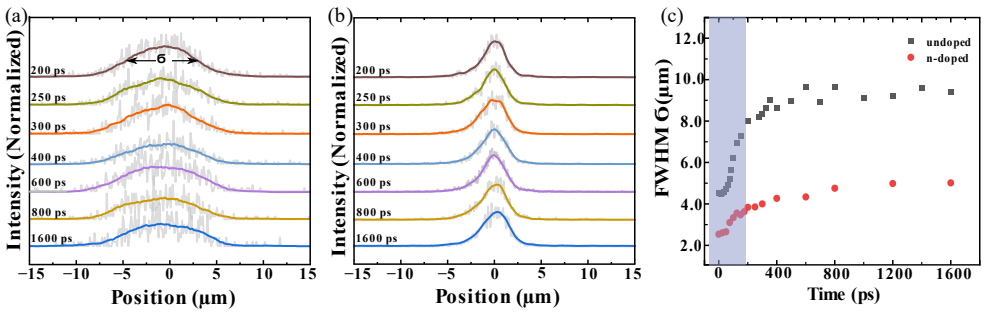

Figure. 4.15: *Normalized spatial profiles, captured at various points in time after the excitation. These plots illustrate the spatial distribution of IX emission at different temporal intervals after the pulse excitation for (a) an undoped platelet and (b) a doped platelet. PL intensity integrated over time windows of 25 ps. (c) Measured FWHM of the IX emission peak vs. time for an undoped (black) and doped (red) platelet. Exclusion of data before 200 ns, indicated by the shaded region, in the temporal evolution of the spatial distribution of IXs.*

The temporal evolution of the IXs after the excitation is depicted in Figs 4.15(a) and 4.15(b) for undoped and n-type doped platelets, respectively. An initial qualitative comparison of these expansions corresponding to the time traces reveals a larger expansion of IXs in the undoped case compared with the doped one. For a clearer

visualization and more quantitative analysis of the expansion behavior, the temporal evolution of the FWHM of the spatially resolved emission profile is presented in Fig 4.15(c). This observation aligns well with the power-dependent SSPL results presented in Fig 4.13(c), as the presence of numerous electrons from doping screens the repulsive interaction of the IXs, leading to a shorter overall transport distance and a smaller initial expansion even at high IX densities directly after the excitation pulse.

We expect, based on the findings from the spatially resolved SSPL results, that under high EPD, the spatial distribution of the IX emission in undoped platelets is influenced by Coulomb repulsion, resulting in a more widespread distribution. Conversely, at lower EPD, the spatial distribution of the IX emission becomes diffusive, leading to a narrower spatial distribution. This trend is clearly depicted in Fig 4.15(c), demonstrating the initial rapid expansion of the IXs immediately after the laser pulse in the undoped platelet. In the initial phase, characterized by a high IX density post-excitation, repulsive interactions among aligned IX dipoles prompt a rapid expansion of the IXs away from the excitation spot. This results in a broader expansion during the initial period (< 200 ps) in the undoped case. As time progresses, the IX density diminishes, and the behavior transitions to a linear pattern, indicating an increasing influence of diffusive-driven transport.

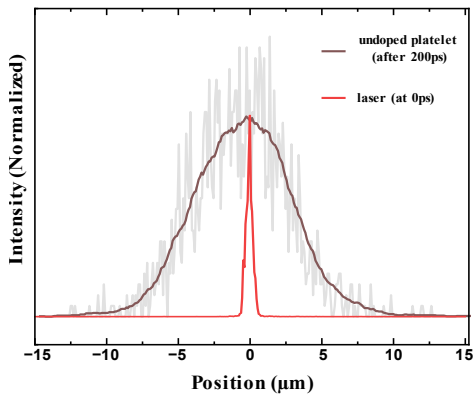

Figure 4.16: *Normalized spatial profiles of the laser spot with PL intensity of IXs for an undoped (a) platelet. The spatial profile of the laser is captured at t = 0 ps, while the spatial profile of the IXs is obtained at t = 200 ps after the pulse excitation.*

To evaluate the rapid expansion of the IXs before 200 ps, we compare the spatial profile of the laser spot at t = 0 with the spatial profile of the IX expansion at 200 ps following the excitation pulse as shown in Fig 4.16. The FWHM of the laser spot is approximately 1 μm, while the FWHM of IX in the undoped sample is 8 μm. The observed 8 μm FWHM suggests the possibility of IX expansion before 200 ps.

However, the temporal and spectral resolution of our streak system lacks the resolution to conclusively confirm this occurrence as we cannot record the entire IX emission and simultaneously exclude the emission from the bulk excitons. Consequently, the extracted velocity value provides a lower limit of the actual expansion velocity. We find a minimum expansion velocity of the IXs of about 1,750,000 cm/s, compared with the electron saturation velocity of 6,800,000 cm/s in InP[67]. This comparison leads us to conclude that scattering from interface fluctuations is of low importance in our system.

Conclusion & Outlook

Polytype heterostructures, formed by engineering crystal structures within the same material, present distinct advantages over traditional heterostructures composed of different compounds. Conventional heterostructures often encounter challenges like interface roughness and compositional intermixing, which can impact their optical properties. In contrast, polytype heterojunctions enable the creation of well-defined interfaces between wz or zb crystal structures in e.g., InP. This interface acts as an electron-hole separator, facilitating the study of IX formation. To explore the physical properties of IXs at type-II interfaces, non-destructive photoluminescence spectroscopy has been employed. To investigate the recombination and spatial dynamics of IXs at the single type-II wz/zb interface, two types of nanostructures are studied in this thesis.

1. The first type of nanostructure consists of nominally undoped wz/zb NWs with typical diameters on the order of tens of nanometers. These have an average wz length of 2 μm, with a zb top segment of around 200 nm. The study in Paper-I centers on recombination dynamics of IXs at the single wz/zb interface in InP NWs.
2. The second type of nanostructure, platelets, overcome the small cross-section limitation of NWs (< 1 μm^2). These platelets have a substantially larger interface cross-section (> 500 μm^2) with a thin, flat InP wz layer on top of a zb InP substrate, offering a larger sample for investigating the spatial distribution of IX. Paper-II and Paper-III explore IX dynamics at the wz/zb single-interface of platelets.

In addition to investigating the behavior of undoped nanostructures, our study delves into the influence of a 2DEG on the recombination and spatial dynamics of IXs in n-type doped nanostructures. These structures maintain an identical geometry to the undoped ones, with the exception that the entire wz segment is degenerately n-type doped.

The principal findings of this thesis include:

1. The IX emission exhibits a redshift as the CW laser EPD decreases. In undoped platelets, the IX emission peak undergoes a substantial redshift of approximately 30 meV, while in n-type doped platelets, a much smaller redshift of only 10 meV is observed, despite a similar change in EPD. These

results offer compelling evidence for the presence of an electron gas induced by doping.

2. In contrast to the bulk excitons in the wz and zb segments, the decay profile of the IX emission exhibits a non-exponential characteristic. A significant intensity of IX emission persists even after 30 ns for undoped NW; conversely, in undoped platelets, this emission remains observable even 40 μs after excitation pulse. Additionally, a redshift in the peak energy of the IX emission, with an approximate 50 meV shift over time, is observed. This shift correlates with a faster recombination at high energy levels (1.45 eV) and a slower recombination rate at lower energy levels (1.42 eV), supporting the time-dependent wavefunction overlap hypothesis. The decay profiles of IX emission in n-type doped nanostructures suggest a higher recombination rate as the presence of numerous electrons per hole enhances the overall recombination process.
3. The spatially resolved PL reveals that the transport of IXs at the undoped type-II interface of the platelet is EPD-dependent. The broad spatial distribution of IX emission indicates that transport is repulsive-force-driven at high EPD and the narrow spatial distribution at low EPD suggests a diffusive transport mechanism. In contrast, the transport of excitons in the wz and zb segments is diffusive and EPD-independent. The spatial profile of IX emission in the n-type doped platelet is narrower than in the undoped platelet and is independent of the EPD.
4. The spatially resolved TRPL reveals an initial rapid expansion of IXs in undoped platelets during the initial period (< 200 ps), driven by Coulomb repulsion, resulting in a more widespread distribution. Conversely, later in time, it transitions into a linear expansion of the spatial distribution of IXs, indicating diffusive-driven transport. The extracted minimum velocity of about 1,750,000 cm/s for IXs suggests negligible influence of scattering from interface fluctuations in our system.

These findings serve as a basis for exploring various physical phenomena. However, further experiments are essential to address the questions that have arisen during this investigation. Improving temporal and spectral resolution can provide more accurate values for the IX mobility and offer insights into the capture time of electrons and holes in the potential wells. A different measurement approach, cathodoluminescence imaging, offers a comparable method for measuring diffusion. Conducting temperature-dependent experiments can unveil the activation energy of charge carriers, providing valuable insights into the depth of the potential well. Furthermore, delving into unexplored parameters of the pure wz top segment from the platelet becomes feasible, addressing the challenges associated with obtaining such a large wz structure. In terms of transport studies, it becomes possible to investigate the quantum Hall effect by subjecting the samples to high magnetic

fields. Additionally, considering different structural fabrication viewpoints, it becomes feasible to fabricate coupled quantum dots and measure the coherence of excitons within these quantum dots using ultrafast transient photoluminescence. In summary, experimental studies present an opportunity to unravel more fundamental properties of the wz/zb interface and pure wz. It would be highly beneficial to complement this experimental work with theoretical calculations to extract parameters that yield accurate band structures for both crystal structures.

References

1 Paranthaman, M. P., Wong-Ng, W. & Bhattacharya, R. N. *Semiconductor materials for solar photovoltaic cells*. Vol. 218 (Springer, 2016).

2 Schubert, E. F. *Light-Emitting Diodes (2006)*. (E. Fred Schubert, 2006).

3 Streetman, B. G. & Banerjee, S. *Solid state electronic devices*. Vol. 4 (Prentice hall New Jersey, 2000).

4 Mimura, T., Hiyamizu, S., Fujii, T. & Nanbu, K. A new field-effect transistor with selectively doped GaAs/n-AlxGa1-xAs heterojunctions. *Japanese journal of applied physics* **19**, L225 (1980).

5 Sze, S. M., Li, Y. & Ng, K. K. *Physics of semiconductor devices*. (John wiley & sons, 2021).

6 Li, P. *et al.* Recent advances in focused ion beam nanofabrication for nanostructures and devices: Fundamentals and applications. *Nanoscale* **13**, 1529-1565 (2021).

7 Bhattacharya, P. *Semiconductor optoelectronic devices*. (Prentice-Hall, Inc., 1997).

8 Chang, M.-H., Das, D., Varde, P. V. & Pecht, M. Light emitting diodes reliability review. *Microelectronics Reliability* **52**, 762-782 (2012).

9 Wilson, B. A. Carrier dynamics and recombination mechanisms in staggered-alignment heterostructures. *IEEE journal of quantum electronics* **24**, 1763-1777 (1988).

10 Wang, J. *et al.* Evidence of Type-II Band Alignment in III-nitride Semiconductors: Experimental and theoretical investigation for In0. 17Al0. 83N/GaN heterostructures. *Scientific reports* **4**, 6521 (2014).

11 Böhrer, J., Krost, A. & Bimberg, D. Carrier dynamics in staggered-band lineup n-InAlAs/n-InP heterostructures. *Applied physics letters* **64**, 1992-1994 (1994).

12 Wilson, B. *et al.* Recombination mechanisms in type II (GaAs/AlAs) heterostructures. *Journal of Vacuum Science & Technology B: Microelectronics Processing and Phenomena* **6**, 1156-1160 (1988).

13 Mikhailova, M., Moiseev, K., Voronina, T., Lagunova, T. & Yakovlev, Y. P. Transition from the type-II broken-gap heterojunction to the staggered one in the GaInAsSb/InAs (GaSb) system. *Semiconductors* **41**, 161-166 (2007).

14 Vainorius, N. *et al.* Observation of type-II recombination in single wurtzite/zinc-blende GaAs heterojunction nanowires. *Physical Review B* **89**, 165423 (2014).

15 Tedeschi, D. *et al.* Hole and electron effective masses in single InP nanowires with a wurtzite-zincblende homojunction. *ACS nano* **14**, 11613-11622 (2020).

16 Geijselaers, I., Lehmann, S., Dick, K. A. & Pistol, M.-E. Two-dimensional electron gas at wurtzite–zinc-blende InP interfaces induced by modulation doping. *Applied Physics Letters* **116** (2020).

17 Hillmer, H., Forchel, A., Sauer, R. & Tu, C. Interface-roughness-controlled exciton mobilities in GaAs/Al 0.37 Ga 0.63 As quantum wells. *Physical Review B* **42**, 3220 (1990).

18 Tan, C.-K., Sun, W., Wierer, J. J. & Tansu, N. Effect of interface roughness on Auger recombination in semiconductor quantum wells. *AIP Advances* **7** (2017).

19 Lu, I.-L., Wu, Y.-R., Hinckley, J. M. & Singh, J. in *Gallium Nitride Materials and Devices V.* 277-284 (SPIE).

20 Christen, J., Grundmann, M. & Bimberg, D. Scanning cathodoluminescence microscopy: A unique approach to atomic-scale characterization of heterointerfaces and imaging of semiconductor inhomogeneities. *Journal of Vacuum Science & Technology B: Microelectronics and Nanometer Structures Processing, Measurement, and Phenomena* **9**, 2358-2368 (1991).

21 Jancu, J.-M. *et al.* Type II heterostructures formed by zinc-blende inclusions in InP and GaAs wurtzite nanowires. *Applied Physics Letters* **97** (2010).

22 Lehmann, S., Wallentin, J., Jacobsson, D., Deppert, K. & Dick, K. A. A general approach for sharp crystal phase switching in InAs, GaAs, InP, and GaP nanowires using only group V flow. *Nano letters* **13**, 4099-4105 (2013).

23 Bimberg, D., Böhrer, J. & Krost, A. Large oscillator strength of spatially indirect electron–hole recombination at type II heterojunctions: The InAlAs/InP case. *Journal of Vacuum Science & Technology A: Vacuum, Surfaces, and Films* **12**, 1039-1044 (1994).

24 Zrenner, A. *et al.* Indirect excitons in coupled quantum well structures. *Surface science* **263**, 496-501 (1992).

25 Hilton, D., Prasankumar, R. & Taylor, A. Optical Techniques for Solid-State Materials Characterization. *Optical Techniques for Solid-State Materials Characterization*, 329-370 (2012).

26 Alfano, R. R. *Semiconductors Probed by Ultrafast Laser Spectroscopy Pt II*. (Elsevier, 2012).

27 Johansson, J. & Dick, K. A. Recent advances in semiconductor nanowire heterostructures. *CrystEngComm* **13**, 7175-7184 (2011).

28 Jia, C., Lin, Z., Huang, Y. & Duan, X. Nanowire electronics: from nanoscale to macroscale. *Chemical reviews* **119**, 9074-9135 (2019).

29 Zhang, L. *et al.* Wide InP nanowires with wurtzite/zincblende superlattice segments are type-II whereas narrower nanowires become type-I: An atomistic pseudopotential calculation. *Nano letters* **10**, 4055-4060 (2010).

30 Spirkoska, D. *et al.* Structural and optical properties of high quality zinc-blende/wurtzite GaAs nanowire heterostructures. *Physical Review B* **80**, 245325 (2009).

31 Pemasiri, K. *et al.* Carrier dynamics and quantum confinement in type II ZB-WZ InP nanowire homostructures. *Nano letters* **9**, 648-654 (2009).

32 Vörös, Z., Balili, R., Snoke, D., Pfeiffer, L. & West, K. Long-distance diffusion of excitons in double quantum well structures. *Physical review letters* **94**, 226401 (2005).

33 Timofeev, V. & Gorbunov, A. Bose-Einstein condensation of dipolar excitons in double and single quantum wells. *physica status solidi c* **5**, 2379-2386 (2008).

34 Grundmann, M. *Physics of semiconductors*. Vol. 11 (Springer, 2010).

35 Neamen, D. A. & Biswas, D. *Semiconductor physics and devices*. (McGraw-Hill higher education United States, 2011).

36 Peter, Y. & Cardona, M. *Fundamentals of semiconductors: physics and materials properties*. (Springer Science & Business Media, 2010).

37 Bimberg, D., Hess, K., Lipari, N., Fischbach, J. & Altarelli, M. Free excitons in InP in high magnetic fields. *Physica B+ C* **89**, 139-142 (1977).

38 Fox, M. (American Association of Physics Teachers, 2002).

39 Guzelian, A. *et al.* Synthesis of size-selected, surface-passivated InP nanocrystals. *The Journal of Physical Chemistry* **100**, 7212-7219 (1996).

40 Sharma, B. & Purohit, R. *Semiconductor heterojunctions*. Vol. 5 (Elsevier, 2015).

41 Vasko, F. T. & Kuznetsov, A. V. *Electronic states and optical transitions in semiconductor heterostructures*. (Springer Science & Business Media, 1998).

42 David, A. & Miller, B. in *Quantum Dynamics of Simple Systems* 239-266 (CRC Press, 2020).

43 Lehmann, S., Wallentin, J., Jacobsson, D., Deppert, K. & Dick, K. A. A general approach for sharp crystal phase switching in InAs, GaAs, InP, and GaP nanowires using only group V flow. *Nano Lett* **13**, 4099-4105, doi:10.1021/nl401554w (2013).

44 Yeh, C.-Y., Lu, Z., Froyen, S. & Zunger, A. Zinc-blende–wurtzite polytypism in semiconductors. *Physical Review B* **46**, 10086 (1992).

45 Chen, I.-J. *et al.* Conduction band offset and polarization effects in InAs nanowire polytype junctions. *Nano letters* **17**, 902-908 (2017).

46 Jash, A. *et al.* Time-resolved photoluminescence studies of single interface wurtzite/zincblende heterostructured InP nanowires. *Applied Physics Letters* **120** (2022).

47 Jash, A., Lehmann, S., Dick, K. A., Gustafsson, A. & Pistol, M.-E. Excitonic Dynamics at the Type-II Polytype Interface of InP Platelets. *ACS Photonics* **10**, 3143-3148, doi:10.1021/acsphotonics.3c00517 (2023).

48 Shah, J. *Ultrafast spectroscopy of semiconductors and semiconductor nanostructures*. Vol. 115 (Springer Science & Business Media, 2013).

49 Rein, S. *Lifetime spectroscopy: a method of defect characterization in silicon for photovoltaic applications*. Vol. 85 (Springer Science & Business Media, 2005).

50 Caine, E., Subbanna, S., Kroemer, H., Merz, J. & Cho, A. Staggered-lineup heterojunctions as sources of tunable below-gap radiation: Experimental verification. *Applied physics letters* **45**, 1123-1125 (1984).

51 Davies, J. H. *The physics of low-dimensional semiconductors: an introduction*. (Cambridge university press, 1998).

52 Seifert, W. *et al.* Growth of one-dimensional nanostructures in MOVPE. *Journal of Crystal Growth* **272**, 211-220, doi:10.1016/j.jcrysgro.2004.09.023 (2004).

53 Joyce, H. J., Wong-Leung, J., Gao, Q., Tan, H. H. & Jagadish, C. Phase perfection in zinc Blende and Wurtzite III-V nanowires using basic growth parameters. *Nano Lett* **10**, 908-915, doi:10.1021/nl903688v (2010).

54 Caroff, P. *et al.* Controlled polytypic and twin-plane superlattices in iii-v nanowires. *Nat Nanotechnol* **4**, 50-55, doi:10.1038/nnano.2008.359 (2009).

55 Assali, S. *et al.* Exploring Crystal Phase Switching in GaP Nanowires. *Nano Lett* **15**, 8062-8069, doi:10.1021/acs.nanolett.5b03484 (2015).

56 Wallentin, J. *et al.* Probing the wurtzite conduction band structure using state filling in highly doped InP nanowires. *Nano Lett* **11**, 2286-2290, doi:10.1021/nl200492g (2011).

57 Algra, R. E. *et al.* Twinning superlattices in indium phosphide nanowires. *Nature* **456**, 369-372, doi:10.1038/nature07570 (2008).

58 Wallentin, J. & Borgström, M. T. Doping of semiconductor nanowires. *Journal of Materials Research* **26**, 2142-2156, doi:10.1557/jmr.2011.214 (2011).

59 Wagner, R. S. & Ellis, W. C. VAPOR-LIQUID-SOLID MECHANISM OF SINGLE CRYSTAL GROWTH. *Applied Physics Letters* **4**, 89-90, doi:10.1063/1.1753975 (1964).

60 Staudinger, P., Mauthe, S., Moselund, K. E. & Schmid, H. Concurrent Zinc-Blende and Wurtzite Film Formation by Selection of Confined Growth Planes. *Nano Lett* **18**, 7856-7862, doi:10.1021/acs.nanolett.8b03632 (2018).

61 Staudinger, P., Moselund, K. E. & Schmid, H. Exploring the Size Limitations of Wurtzite III–V Film Growth. *Nano Letters* **20**, 686-693, doi:10.1021/acs.nanolett.9b04507 (2020).

62 O'Connor, D. *Time-correlated single photon counting*. (Academic press, 2012).

63 Egerton, R. F. *Physical principles of electron microscopy*. Vol. 56 (Springer, 2005).

64 Magnusson, M. H., Deppert, K., Malm, J.-O., Bovin, J.-O. & Samuelson, L. Size-selected gold nanoparticles by aerosol technology. *Nanostructured Materials* **12**, 45-48 (1999).

65 Feller, W. *An introduction to probability theory and its applications, Volume 2*. Vol. 81 (John Wiley & Sons, 1991).

66 Wallentin, J. *et al.* Probing the wurtzite conduction band structure using state filling in highly doped InP nanowires. *Nano letters* **11**, 2286-2290 (2011).

67 Quay, R., Moglestue, C., Palankovski, V. & Selberherr, S. A temperature dependent model for the saturation velocity in semiconductor materials. *Materials Science in Semiconductor Processing* **3**, 149-155 (2000).